UNIVERSITÀ DEGLI STUDI DI PADOVA

SCUOLA DI SCIENZE
Dipartimento di Geoscienze
Direttore Prof. Fabrizio Nestola

TESI DI LAUREA MAGISTRALE
IN
GEOLOGIA E GEOLOGIA TECNICA

EXPLOITATION OF UNSUITABLY ORIENTED FOLIATION BY LOCALIZED MYLONITES AND PSEUDOTACHYLYTES (TAUERN WINDOW, EASTERN ALPS)

Relatore: Prof. Giorgio Pennacchioni

Laureando: Giovanni Toffol

ANNO ACCADEMICO 2018/2019

ABSTRACT

The focus of my Master thesis is to describe and characterize previously overlooked deformation structures in the meta-granitoids and derived mylonites of the Tauern Window (eastern Alps). This work gave me the opportunity to learn a research approach that goes from the macro scale to the micro scale, combining field survey and advanced laboratory techniques. The research has potential implication in the understanding the interplay between earthquake rupturing (recorded by pseudotachylytes) and ductile flow (recorded by mylonites) at the base of the brittle crust during the seismic cycle. The thesis work has included: (i) a campaign of field work with detailed mapping and photographic recording (by drone and on-ground survey), at different scales, of the outcrops; (ii) elaboration of high-resolution 3D photomosaic by photogrammetric techniques quantitatively reconstructing the meso-scale deformation network; and (iii) microstructural and petrographic analysis of samples including a detailed quantitative study of the fabric of recrystallized quartz in mylonites.

The rocks studied during the thesis come from the front of the southern Mesule glacier where outcrops are perfectly exposed on glacier-polished surfaces ideal for the structural field analysis. This area exposes large portions of Tauern meta-granitoids, derived from upper Carboniferous intrusions, that are preserved in a low strain domain just north of a major Alpine amphibolite-facies mylonitic zone forming the southern boundary of the tectonic unit. Within the low strain domain Alpine deformation is mainly localized to a network of small scale (cm-dm-thick) strike slip ductile shear zones, and to few thicker (a few meter wide) mylonitic bands (*Mancktelow and Pennacchioni 2005; Pennacchioni and Mancktelow, 2007*). The amphibolite facies foliation and shear zones are cut by a pervasive set of conjugate epidote-chlorite-bearing shear fractures, faults and associated extensional veins whose orientation and kinematics is consistent with a ca. N-S shortening direction during cooling of the Tauern units at conditions close to the brittle-ductile transition (ca. 300 °C) (*Pennacchioni and Mancktelow, 2007*).

The deformation structures, referred to as *Stage-2* structures, investigated in the present thesis developed between the main amphibolite facies ductile stage (*Stage-1*) and the later brittle stage (*Stage-3*) of faulting and veining. *Stage-2* structures have been identified within 3 majors (several meters thick) mylonitic zones and consist of narrow mylonites and pseudotachylytes exploiting the pervasive foliation of the host *Stage-1* mylonites:

i. *Stage-2* mylonites are sharply-bounded, black-coloured horizons, of as much as few cm thick, changing in kinematics with respect to the former *Stage-1* mylonite
ii. Pseudotachylytes (quenched frictional melts) are discontinuous thin (mm-thick) faults veins, with local injections, that are closely associated with *Stage-2* mylonites along the same structural surfaces.

The perfect exposure on polished surfaces has allowed the geometry and extension of these structures to be mapped in detail. The maps representing the geometry of the *Stage-2* structures have been constructed based on the huge collection of overlapping high-resolution photographs (1 pixel < 1 cm). With the photogrammetry software Agisoft, georeferenced orthophotographs have been built and used for map drawing in ArcGis.
Stage-2 structures are continuous over large distances along strike (tens to hundred meters) and are clearly offset by *Stage-3* faults and veins. The kinematics and orientation of *Stage-2* structures constrain the regional shortening direction to orientations close to that during *Stage-1,3* deformations. Given the high angle orientation of the *Stage-1* mylonitic foliation to the shortening direction, we inferred that the resolved shear stress during *Stage-2* exploitation of the precursor foliation was low.

The sample analysis has included: (i) optical and SEM (BSC: back-scattered electron mode) microscopy; (ii) SEM-EDS compositional semi-quantitative analysis; and (iii) determination by electron backscattered diffraction (EBSD) of crystallographic preferred orientation (CPO) of quartz of *Stage-2* mylonites and pseudotachylytes. EBSD data post-processing involved intensive learning of the MatLab-based open-source MTEX software (https://mtex-toolbox.github.io/). The aim of this analysis was to investigate the ambient conditions of development of *Stage-2* deformation and the relationships between mylonites and pseudotachylytes. The main results of the analyses are:

a. *Stage-2* mylonites developed under greenschist facies metamorphic conditions with the main foliation outlined by syn-kinematic growth of biotite, epidote and plagioclase (oligoclase). Garnet was apparently not stable during deformation.
b. *Stage-2* mylonitization was associated with extensive grain size reduction by dynamic subgrain rotation recrystallization of coarse (mm-sized) quartz of precursor amphibolite facies mylonites. Grain size of newly recrystallized quartz, determined from EBSD maps, is variable and ended up in ca. 3 μm grain diameters within the most highly strained aggregates.
c. The CPO's of dynamically recrystallized quartz is characterized by a pole figure with peripheral *c*-axis maximum; inverse pole figures suggests the activity of

different slip systems for low misorientation angles, but a dominant rhomb <a> slip for recrystallized *Stage-2* quartz aggregates.

d. The EBSD-calibrated paleopiezometer (*Cross et al. 2017*) yields high differential stress of more than 200 MPa.
e. Pseudotachylytes do not show evidence of a ductile overprint while they cut the mylonites; quartz in the host rock selvages, immediately adjacent to fault veins, exhibits an ultrafine recrystallization to grainsizes comparable with that of *Stage-2* mylonites.

The close spatial association determined in the field between *Stage-2* mylonites and pseudotachylytes and the microstructural features together suggest a cogenetic development of localized high stress flow and frictional melting. We propose a process that, thanks to a mylonitic-driven rearrangement of the fabric, weaken the foliation allowing frictional slip along highly misoriented anisotropies to take place.

RIASSUNTO

Lo scopo della mia tesi di laurea è di descrivere e caratterizzare delle strutture deformative precedentemente trascurate nei metagranitoidi della Finestra dei Tauri (Alpi orientali). Questo lavoro mi ha dato la possibilità di imparare un metodo di ricerca a diverse scale, combinando osservazioni sul campo e analisi di laboratorio avanzate. La ricerca presenta potenziali implicazioni nella comprensione delle interazioni tra rottura sismica (registrata dalle pseudotachiliti) e flusso duttile (registrato dalle miloniti) alla base della crosta sismogenica durante il ciclo sismico. Il lavoro di tesi ha incluso: (i) lavoro sul campo con mappatura di dettaglio e acquisizione di fotografie degli affioramenti a diverse scale (sia con l'utilizzo di un drone che sull'affioramento); (ii) elaborazione di fotomosaici ad alta risoluzione per ricostruire il network deformativo alla mesoscala; (iii) analisi microstrutturali e petrografiche volte a studiare il fabric di ricristallizzazione del quarzo nelle miloniti.

Il luogo interessato da questo studio si trova alla fronte del ghiacciaio delle Mesule, dove gli affioramenti, perfettamente lucidati dal ghiacciaio, rappresentano la situazione ideale per studi strutturali sul campo. In quest'area affiorano grandi porzioni dei metagranitoidi dei Tauri, derivati da intrusioni del Carbonifero superiore, preservate in un dominio di low strain situato a nord di una importante zona milonitica alpina che costituisce il confine meridionale dell'unità tettonica. All'interno del dominio di low strain la deformazione alpina è concentrata in un network di piccole (cm – dm) zone di shear duttile e in alcune fasce milonitiche più spesse (qualche metro) (*Mancktelow and Pennacchioni 2005; Pennacchioni and Mancktelow, 2007*). La foliazione anfibolitica e le zone di shear sono tagliate da un set pervasivo di fratture e faglie ad epidoto-clorite e dalle associate vene estensionali, le cui orientazioni e cinematica sono consistenti con una direzione di raccorciamento ca. N-S durante il raffreddamento dell'unità dei Tauri in condizioni prossime alla transizione duttile-fragile (ca. 300°C) (*Pennacchioni and Mancktelow, 2007*).

Le strutture deformative (*Stage-2*) studiate in questa tesi si sono sviluppate tra la principale fase duttile in facies anfibolitica (*Stage-1*) e la successiva fase fragile (*Stage-3*). Le strutture dello *Stage-2* sono state identificate in tre zone milonitiche principali (dello spessore di diversi metri) e sono costituite da sottili miloniti e pseudotachiliti che sfruttano la foliazione pervasiva delle miloniti dello *Stage-1*:

i. Le miloniti dello *Stage-2* sono orizzonti di colore scuro e con margini netti, spessi al più qualche cm, con una cinematica opposta rispetto a quella della milonite di *Stage-1*

ii. Le pseudotachiliti si trovano in venette di fuso spesse qualche mm e discontinue, con locali iniezioni e intimamente associate alle miloniti dello *Stage-2*

La mappatura di dettaglio delle geometrie e dell'estensione delle strutture è stata possibile grazie all'eccellente lucidatura degli affioramenti. Le mappe sono state ottenute a partire da una grande quantità di immagini ad alta risoluzione (1 pixel < 1 cm) elaborate con il software di fotogrammetria Agisoft, con il quale sono state prodotte ortofoto georeferenziate importabili su ArcGis.

Le strutture dello Stage-2 sono continue per grandi distanze (decine, centinaia di metri) e tagliate da vene e faglie dello Stage-3. La cinematica e l'orientazione di queste strutture rappresenta un vincolo per stimare la direzione di raccorciamento regionale durante il loro sviluppo e la pone vicina alla direzione per gli Stage-1,3. Data l'orientazione delle fasce milonitiche lo stress di taglio risolto sul piano di slip doveva essere particolarmente basso.

L'analisi dei campioni ha incluso: (i) microscopia ottica e SEM (modalità back-scattered electrons); (ii) analisi chimiche semiquantitative SEM-EDS; (iii) determinazione tramite analisi EBSD di orientazioni cristallografiche preferenziali del quarzo in miloniti dello *Stage-2*. L'elaborazione dei dati EBSD ha richiesto un approfondito studio del software MTEX, basato su codice MatLab. L'obbiettivo di queste analisi è stato quello di investigare le condizioni in cui hanno avuto luogo le deformazioni dello *Stage-2* e le relazioni tra miloniti e pseudotachiliti. I principali risultati delle analisi sono:

a. Le miloniti di *Stage-2* si sviluppano in condizioni di facies scisti verdi, con la foliazione principale definita dalla crescita sincinematica di biotite, epidoto e plagioclasio (oligoclasio). Il granato non era stabile durante la deformazione.
b. La milonitizzazione è associata a un'intensa riduzione di grana per ricristallizzazione dinamica per subgrain rotation di cristalli di quarzo grossolani (mm) della milonite anfibolitica. La granulometria, determinata da mappe EBSD, è variabile e si attesta attorno ai 3 μm di diametro negli aggregati maggiormente deformati.
c. La CPO del quarzo è caratterizzata da figure polari con massimi periferici degli assi c; le figure polari inverse suggeriscono l'attività di diversi sistemi di slip a basse misorientazioni, dominate dal rombo <a>.

d. L’applicazione di un paleopiezometro (*Cross et al. 2017*) ha fornito valori di stress differenziale superiori a 200 MPa.
e. Le pseudotachiliti non mostrano segni di una sovraimpronta duttile, sono invece osservate tagliare le miloniti; gli aggregati di quarzo nelle immediate vicinanze mostrano ricristallizzazione estremamente fine, con granulometrie comparabili a quelle delle miloniti.

L’associazione tra miloniti e pseudotachiliti determinata sul campo e le evidenze microstrutturali suggeriscono lo sviluppo cogenetico di flusso ad elevato stress e frictional melting. Per giustificare lo slip lungo anisotropie mal orientate proponiamo un processo che prevede un indebolimento della foliazione riattivata guidato dalla deformazione duttile.

INDEX

1. Field Work

The field work during my Master thesis was focused on the identification and characterization of previously overlooked deformation structures of the Neves Area metagranitoids (South Tyrol, eastern Alps). These deformation structures (referred hereafter as *Stage 2* structures) occurred between the two deformation phases well documented in the Neves area (Mancktelow and Pennacchioni, 2005; Pennacchioni and Mancktelow, 2007, 2013, 2018), namely: (i) amphibolite facies ductile deformation responsible for the development of the regional foliation in the Neves granitoids (*Stage 1*); and (ii) brittle faulting and veining associated with the development of the Mesule Fault (Pennacchioni and Mancktelow, 2013) (*Stage 3*).

The field work was addressed at (i) identifying and describing the mesoscale geometric features and "fault rocks" of *Stage 2* deformation; (ii) determining the relationships with previous and later *Stage 1 and Stage 3* deformations; and (iii) mapping in detail the network of *Stage 2* structures. Quantitative mapping was based on an extensive photographic survey (from both on-ground photography and drone photography) that has allowed construction of ultra-detailed (pixel size < 1 cm) 3D outcrop models by photogrammetric techniques and to derive outcrop detailed ortho-photographs of large outcrop areas. During the field campaign, a set of samples, representative of all *Stage* 2 structures and fault rocks, was collected for the successive lab analysis.

1.1 Structural framework of the Neves area

The investigated area is located in the upper Molini Valley (a western tributary valley of the Aurina Valley, Alto Adige, Italy). The studied outcrops are located at the toe of the Mesule Glacier (Fig. 1), where the recent glacier retreat has uncovered perfectly polished outcrops, that allow field investigation of rock details down to the grain scale and is therefore ideal for structural observations and mapping.

The area geologically lies at the south-western border of the Tauern Window granitoid unit. The studied area corresponds to a major low strain domain with respect to the Alpine deformation and it is delimited, to the south, by a kilometric wide mylonitic zone marking the contact between the Penninic ophiolitic nappe and Tauern Window granitoids. In the low strain area, the exposed rocks mainly consist of metagranitoids, with minor mafic and

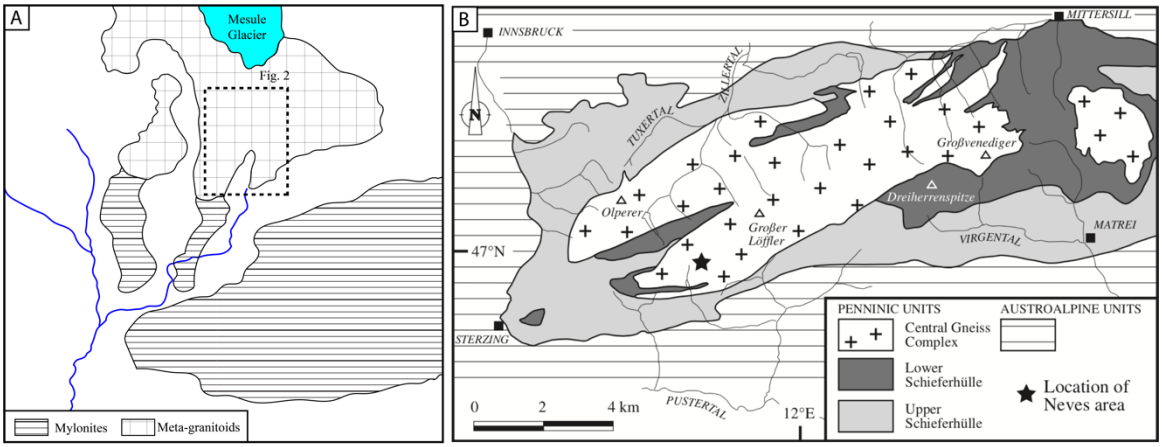

Fig. 1 a) Schematic representation of the Neves Area; b) simplified geological map of the Tauern Window, from Pennacchioni and Mancktelow 2013

felsic dykes, of late-Hercynian age. The main meta-intrusive rocks are medium-grained, equigranular granodiorites (quartz, plagioclase, biotite, with minor K-feldspar and muscovite) dated 295 ± 3 Ma (Cesare, 2002). A magmatic foliation is preserved in the intrusion, marked by the preferred orientation of biotite and by the elongation of mafic xenoliths. This foliation strikes almost north-south and is steeply dipping. After emplacement, the main granodioritic body was intruded by a first generation of mafic dykes (lamprophyre$_1$), of as much as a few meters in thickness, steeply dipping and striking between N and NE. These dykes show magma mingling relationships with the host granodiorite indicative of a coeval age of intrusion. The magma mingling structures are closely associated with fine-grained leucocratic granites, probably representing the re-melting product of the granodiorite at the contact with the hotter mafic magma. Lamprophires$_1$ are crosscut by aplitic dykes of variable orientations. Finally, a younger set of E-W-striking, steeply-dipping mafic dykes (lamprophire$_2$) cut all the previously described structures. These dykes include bodies of as much as 1 km long and 5 m thick. Lamprophires$_2$ generally exhibit sharp boundaries, suggesting that the emplacement conditions were different than for the lamprophire$_1$, at a stage when the host granodiorite was completely solidified.

During the Tauern metamorphism the plutonic bodies of the south-western portion of the Tauern Window underwent a peak temperature of 550 – 600 °C (Hoernes and Friedrichsen, 1974, Selverstone 1985). In the low strain domain of Neves area, the Alpine ductile deformation is localized to a network of small shear zones developed on different tabular discontinuities. After exhumation and cooling above the brittle-ductile transition between Oligocene and Neogene (Selverstone 1988) the Tauern granitoids were affected by a brittle deformation (the *Stage-3*), with the development of shear fractures and veins filled with chlorite, epidote and quartz. The major *Stage-3* structure in the Neves area is represented

by the Mesule Fault (Pennacchioni and Mancktelow, 2013), a strike-slip fault accommodating a maximum left-lateral offsets of about 20 m.

In the following sections, a more detailed description of the *Stage-1* and *Stage-3* structures is reported. The map of Fig. 2 shows the spatial distribution of the structures in the area of interest. The orientation, kinematics and shortening direction of *Stage-1-3* are schematically represented in Fig. 10a. Representative field structures of these deformation stages are shown in the photographic plate of Fig. 3.

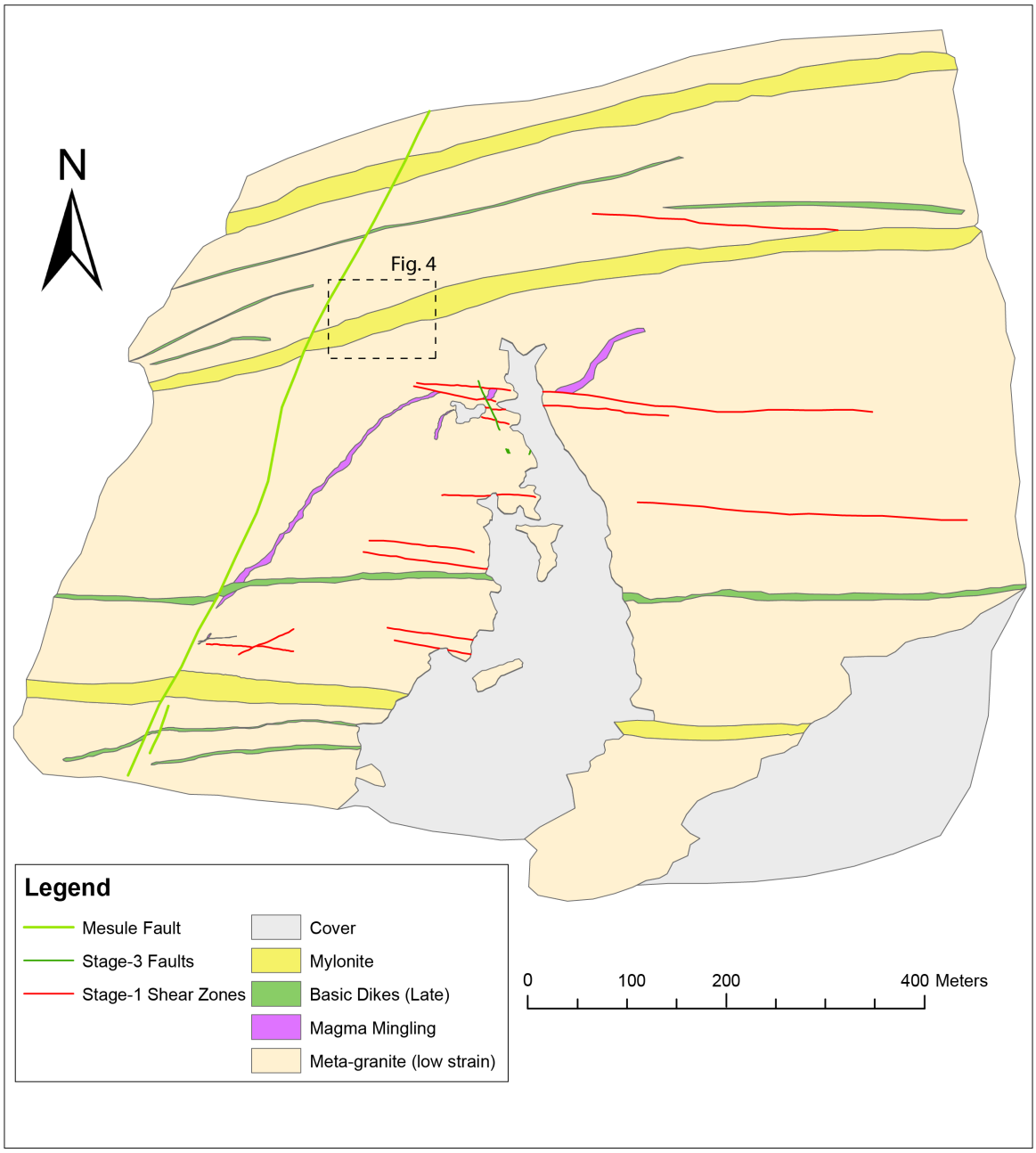

Fig. 2 Geological map of the studied outcrops at front of the southern tongue of the Mesule Glacier in the Neves area.

1.1.1 *Stage-1* deformation

This deformation stage, widely described in *Mancktelow and Pennacchioni* (2005) and *Pennacchioni and Mancktelow* (2007), took place under amphibolite facies conditions and consists of several millimetric- to centimetric-thick (to even metric) ductile shear zones. These localized shear zones exploited tabular precursors, such as brittle fractures, alteration haloes surrounding fractures infiltrated by fluids, dykes and dyke boundaries, and veins. Commonly the shear zones show mutual crosscutting relationships and define a complex pattern of small shear zones within the otherwise weakly deformed meta-granitoids (Fig. 3b, c, d).

During *Stage*-1 deformation, some major, a few meters thick, mylonitic zones developed in the Neves area. At the front of the southern Mesule glacier, there are 3 of these major mylonitic zones hereafter referred to as, from south to north, $Mylonite_1$, $Mylonite_2$ and $Mylonite_3$. These major mylonitic bands can be identified in aerial and satellite images. On the field they can be traced across the whole area.

The shortening direction during *Stage-1* deformation was constrained at 345° N from the change in shear zone kinematics of the differently oriented shear zones (Pennacchioni and Mancktelow, 2007). It is worth of note that, during *Stage-1* deformation, structural anisotropies with any orientation, also including structures almost orthogonal to the shortening direction, were exploited by shear zones, consistently with an almost ideal viscous fluid rheology and very low differential stresses (Mancktelow and Pennacchioni, 2010).

1.1.2 *Stage-3* deformation

This deformation phase, described in *Pennacchioni and Mancktelow* (2013), is linked with the development of the Mesule Fault, a NNE-SSW-striking, steeply dipping sinistral strike-slip fault situated in the west portion of the Neves Area. The deformation event took place under lower greenschist facies, under hydrous conditions approximately at the base of the brittle crust. *Stage-3* structures include conjugate shear fractures and extensional veins crosscutting *Stage-1* structures (Fig. 3e, f). Shear fractures are commonly arranged in conjugate sets with an intersection angle of less than 60° consistent with a relatively high fluid pressure.

The brittle structures show all the stages of the evolution, from thin millimeter size fractures, to a metric fault. These fractures are newly developed structures and very rarely

exploited pre-existing discontinuities. The shortening direction has been calculated by *Pennacchioni and Mancktelow* (2013) at around 358° N.

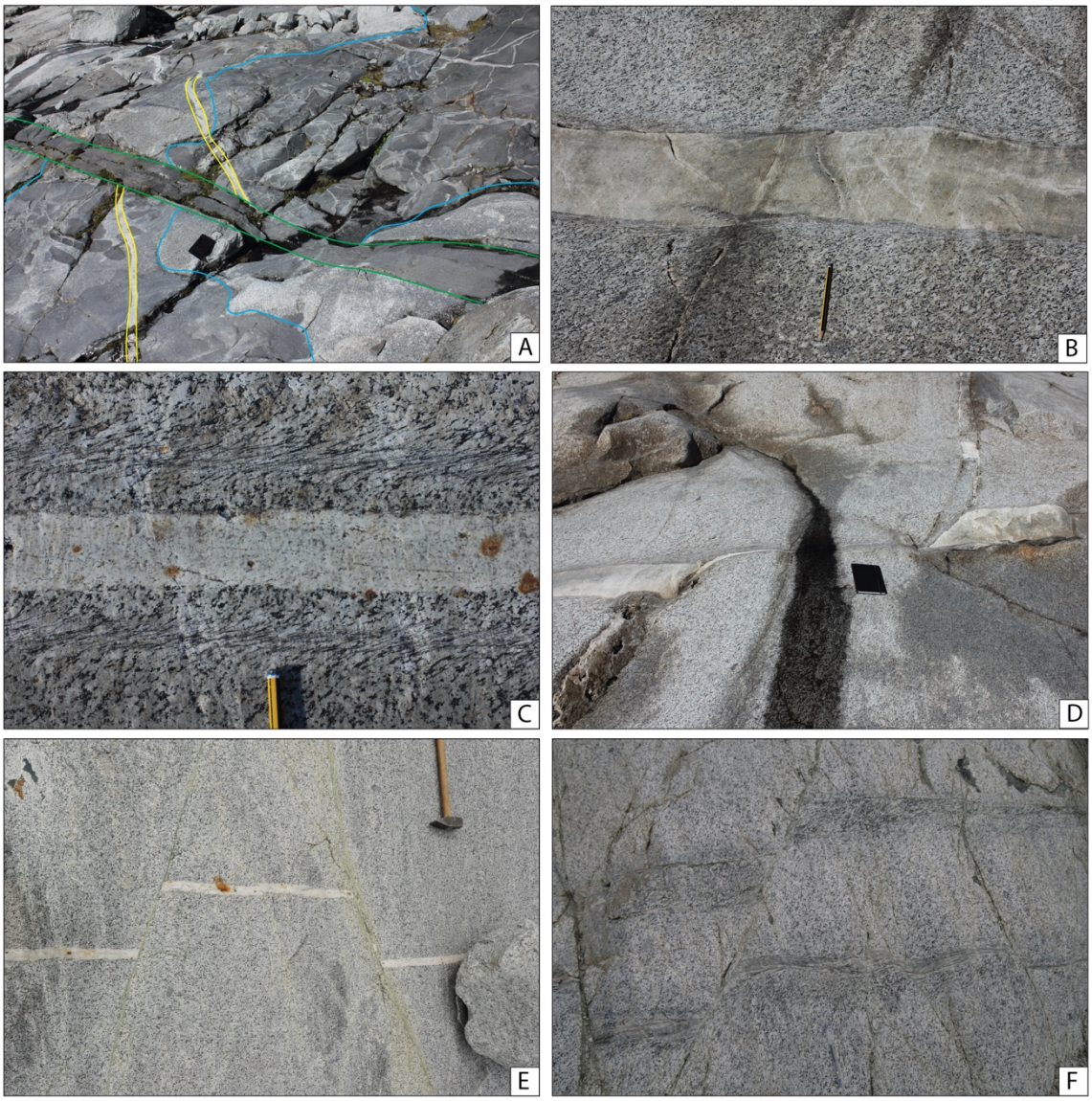

Fig. 3 Stage-1 and Stage-3 field deformation structures: a) different dyke intrusions (blu: magma mingling; yellow: aplite; green: mafic dyke) within the metagranodiorite showing amphibolite facies, dextral shearing (Stage-1) localized on the latest mafic dyke; b) Stage-1 paired shear zones exploiting the borders of an aplite; a thin calcite-quartz filled veins deformed by the paired shear zones indicates that the deformation is clearly localized at the boundaries of the aplite and mainly concentrated in the granodiorite selvages; c) Stage-1paired shear zones localized on a bleached halo around an aplite; d) mutually intersecting Stage-1 shear zones exploiting an aplite dyke and a quartz vein; the simultaneous shearing of the shear zones results in a thinning domain at the intersection; e) Stage-3 conjugate shear fractures offset an aplite dyke; f) Stage-3 fractures crosscutting and offset Stage-1 shear zones.

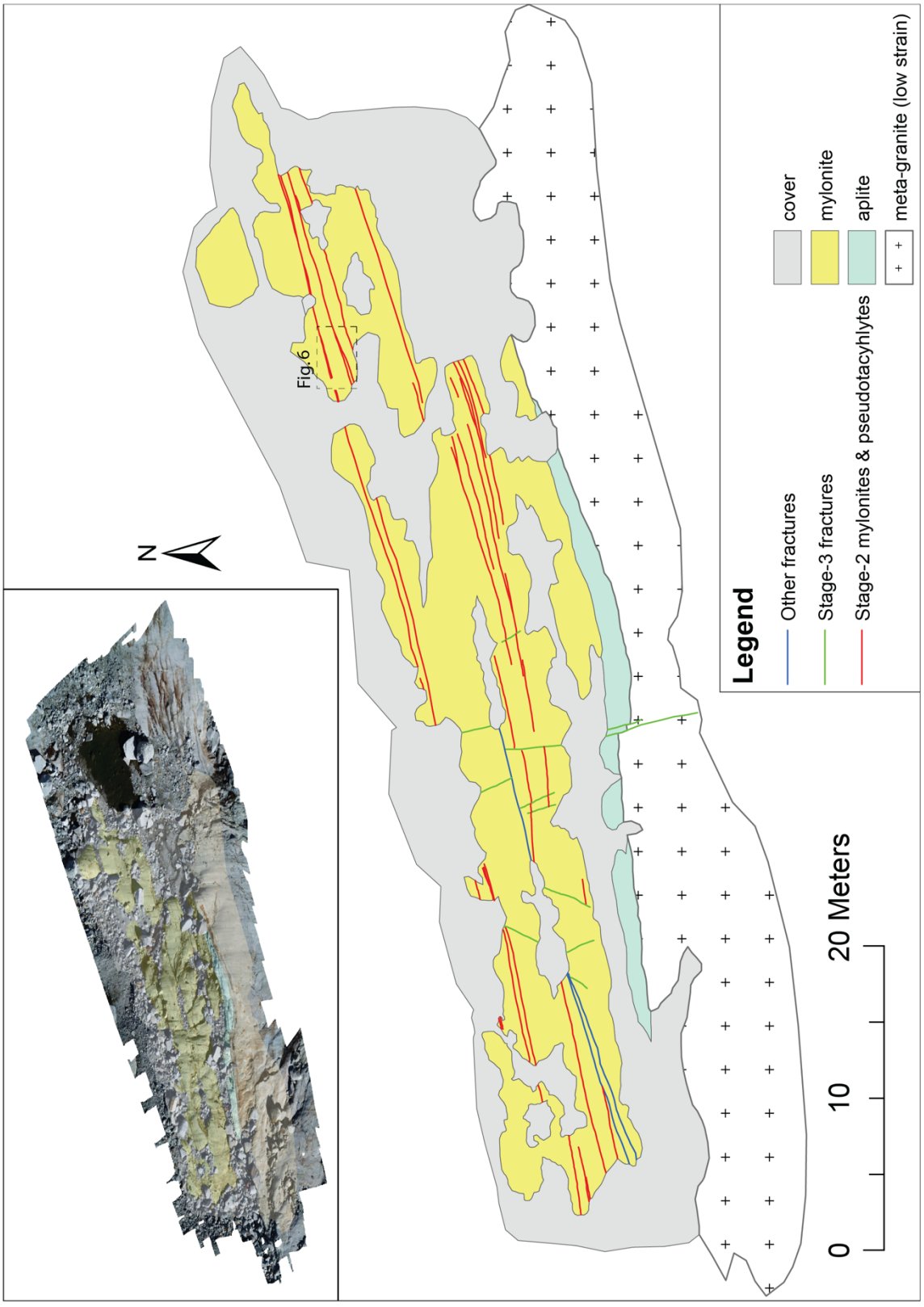

Fig. 4 Detailed map of the distribution of Stage-2 localized mylonites within Mylonite$_2$.

1.2 *Stage-2* DEFORMATION

Stage-2 deformation structures, which are the main investigated structures in this Master study, consist of discrete shear reactivations (both ductile shear zones and pseudotachylytes) of the *Stage-1* mylonitic foliation that were observed in the three mains (several meters thick) mylonitic horizons across the meta-granitoids at the base of the Mesule glacier. As discussed later in the text, *Stage-2* shearing has a different kinematics than the host *Stage-1* mylonites. Potential *Stage-2* reactivations may include the numerous contrasting sense of shear described for paired shear zones between the central sharp fracture/vein and the bounding symmetric pair of heterogeneous shear zones (Pennacchioni and Mancktelow, 2007). This means that *Stage-2* deformation is likely more diffuse than recognized.

At the outcrop scale the *Stage-2* structures appear as mm- to cm-thick, fine grained, dark-colored horizons easily recognizable within the lighter colored and coarser grained *Stage-1* mylonites. These structures are very continuous along the outcrops and can be traced for several meters. The map of Fig. 4 shows the distribution of the dark horizons inside the Mylonite$_2$ and their relations whit *Stage-3* fractures. In several cases the dark-colored horizons are crosscut by the *Stage-3* fractures (Fig. 5). In most of the cases the *Stage-2*

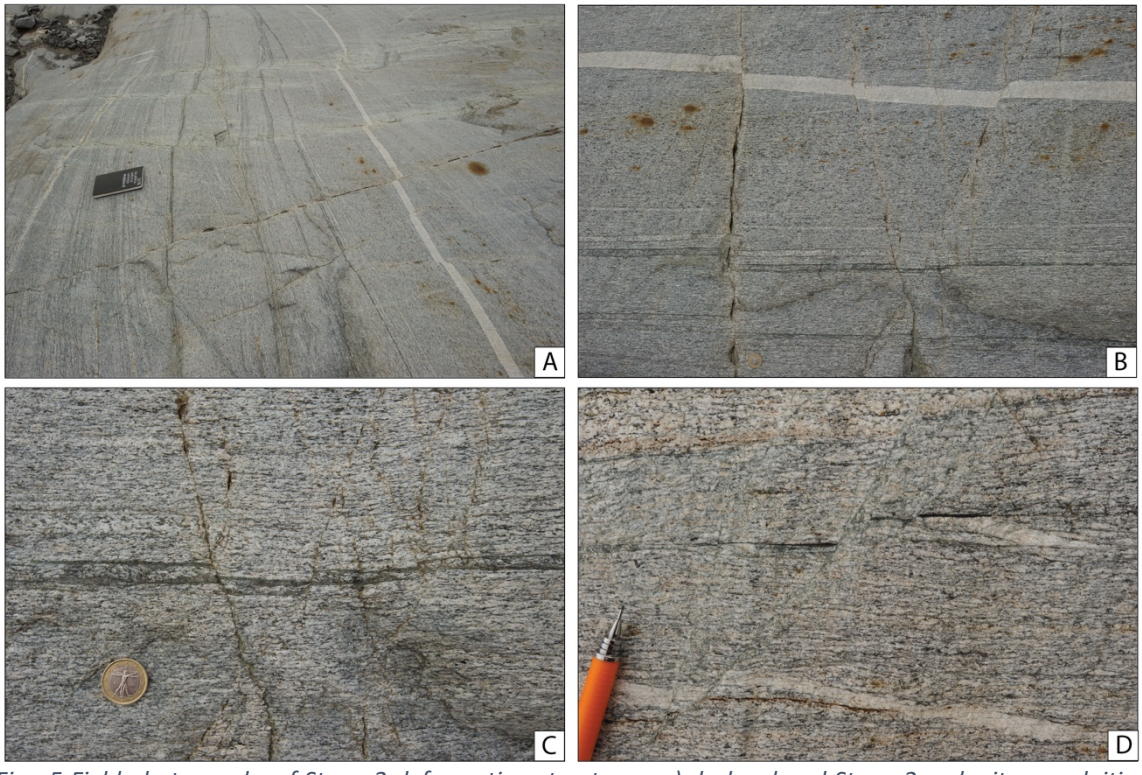

Fig. 5 Field photographs of Stage-2 deformation structures: a) dark-colored Stage-2 mylonites, exploiting the foliation of Mylonite$_3$, crosscut by later Stage-3 small faults; b), c) details of a); d) pseudotachylyte bearing Stage-2 fault in the Mylonite$_2$, crosscut by Stage-3 shear fractures.

structures are parallel to former *Stage-1* foliation but, in other examples, they are slightly discordant to the host foliation and usually converge toward another *Stage-2* subparallel structure. *Stage-2* structures occur either isolated or as sets of subparallel (spaced less than 1 m apart) slip planes. In a few cases closely spaced *Stage-2* structures form together paired detachment surfaces, with the host mylonitic foliation in between strongly kinked or showing a chaotic fabric (Fig. 6).

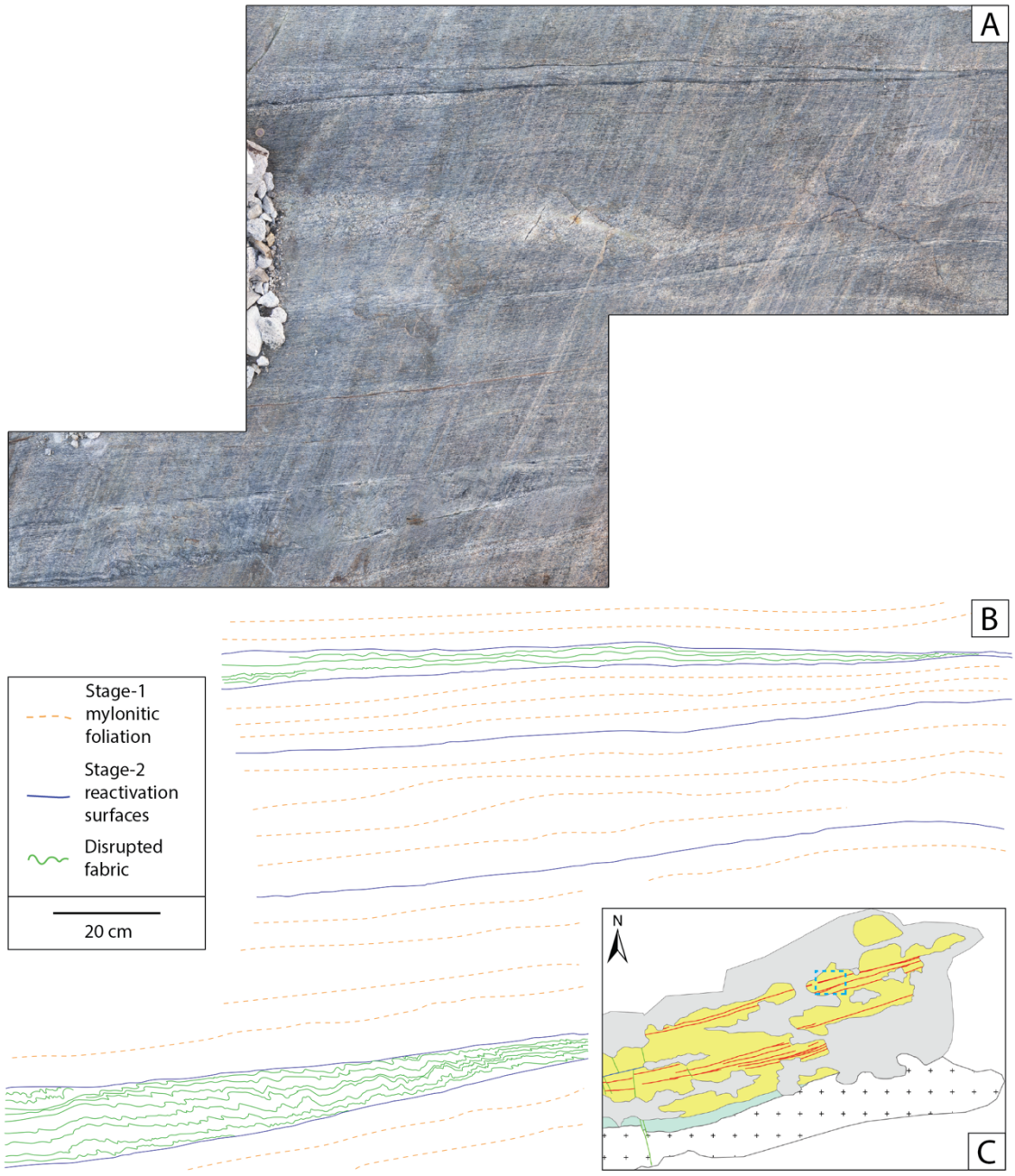

Fig. 6 Stage-2 field deformation structures. Photomosaic (a) and schematic sketch (b) of a set of Stage-2 structures within mylonite2 (see location of the area in the inset (c) reporting the schematic map of the entire western part of the mylonite2 outcrop). In the upper part of the outcrop, 2 subparallel Stage-2 structures acted as detachment surfaces and confine a zone a strongly kinked Stage-2 foliation

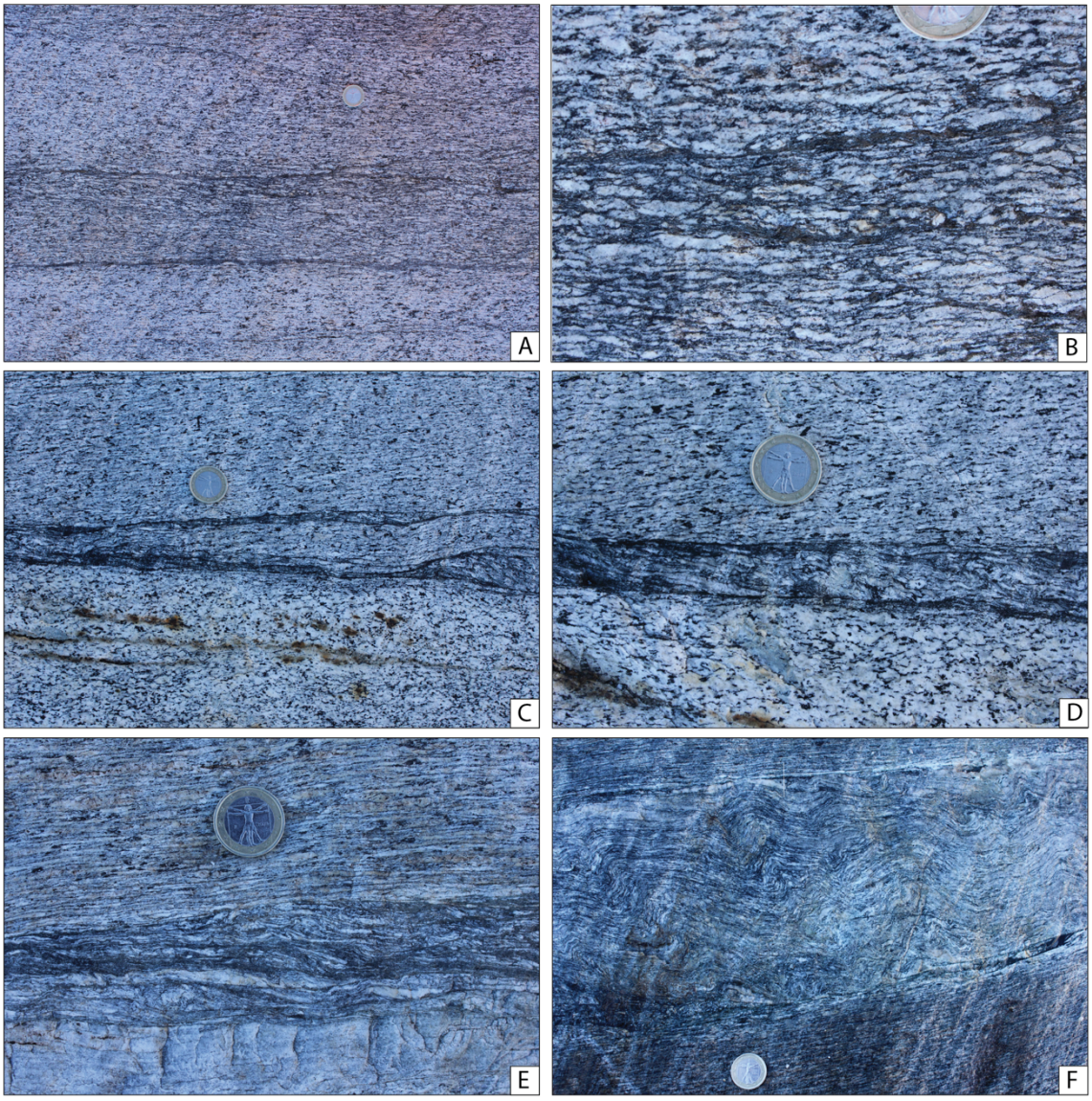

Fig. 7 Field photographs of Stage-2 deformation structures with associated disruption and cataclasis of the Stage-1 foliation; (f) is a detail of the kinked foliation between 2 adjacent Stage-2 slip zones in the outcrop of Fig. 6

To a closer view, *Stage-2* structures typically show relatively sharp boundaries and include both mylonitic (foliation) and cataclastic (disrupted remnants or lithic clasts of the host foliation) features (Fig. 7). Most *Stage-2* structures are identified as localized ductile shear zones with a strong internal foliation, but pseudotachylytes also occur along the same structural planes, including discontinuous mm-thick fault veins and local mm to cm long injection veins typically intruding at a high angle the host foliation (Fig. 8, 9). Pseudotachylytes are present mainly in the Mylonite$_2$, with the presence of typical features (a pull apart filled with melt, a sidewall rip-out (Fig. 8c, d) (Swanson, 1992), but minor occurrence characterizes the reactivation also in Mylonite$_1$ and Mylonite$_3$.

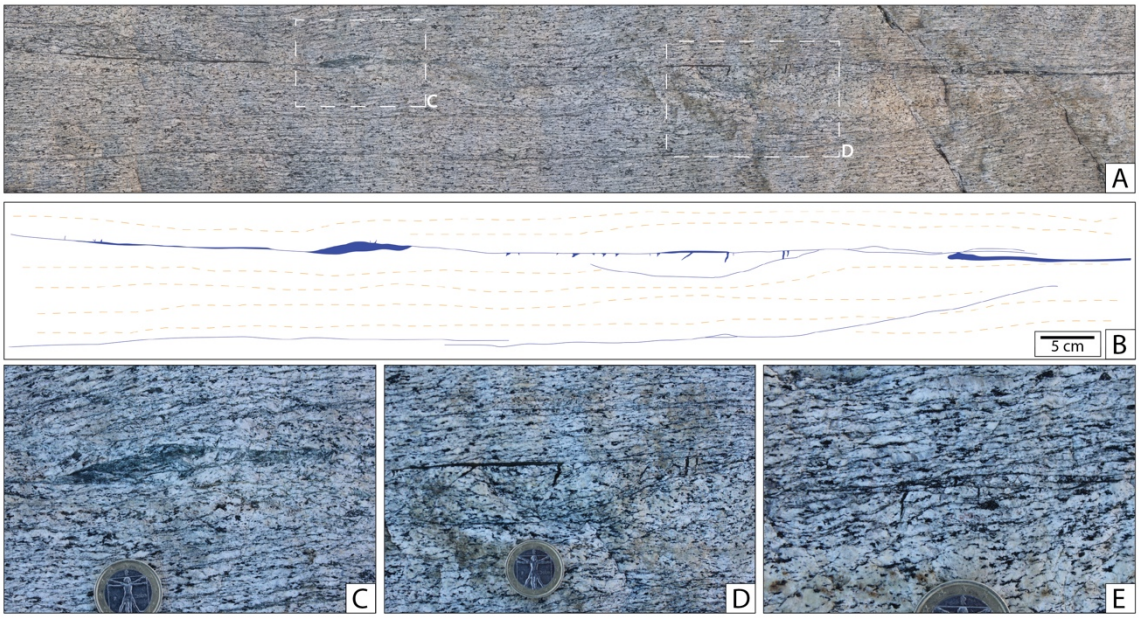

Fig. 8 Photomosaic of a pseudotachylyte-bearing Stage-2 fault in Mylonite$_2$ (a) and interpretative sketch of the pseudotachylyte fault and injection vein geometry (b) Photographic details of the pseudotachylyte vein; (c) pull apart filled with pseudotachylyte consistent with a sinistral strike-slip component of shear; d) sidewall rip-out; e) injection veins intruding the host mylonite

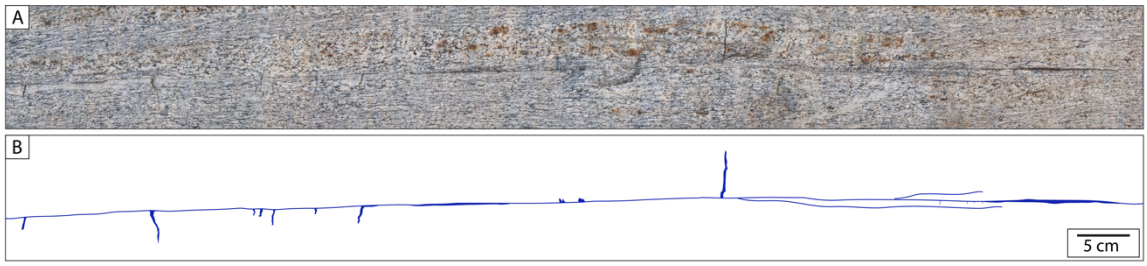

Fig. 9 Photomosaic of a pseudotachylyte-bearing Stage-2 fault in Mylonite2 (a) and interpretative sketch of the pseudotachylyte fault and injection vein geometry (b).

In Mylonite$_3$ the *Stage-2* reactivation affected also the boundaries of an aplitic dyke inside the mylonitized granodiorite, with small pseudotachylyte veins decorating the surfaces. In this case a lineation is present also inside the aplite, indicating that the whole dyke was interested by the deformation.

All the observed structures show a well-developed slikenline-type lineation, clearly distinguished from the high-T mineral lineation of the host mylonites. This lineation, together with the shear sense inferred from the porphyroclasts and foliation asymmetry inside *Stage-2* mylonites, indicate an opposite direction of shearing with respect to the previous *Stage-1* event. The orientations of *Stage-2* mylonitic foliation (and associated lineation) and pseudotachylytes are reported in the stereonet of Fig. 10b and can be summarized as follows:

- Mylonite$_1$: orientation of the pristine foliation around 185-70 (dip direction – dip); *Stage-2* lineation of 090-16 (trend and plunge); dextral shear sense of reactivation.
- Mylonite$_2$ and Mylonite$_3$: pristine foliation oriented around 335-80 (dip direction – dip); the *Stage-2* lineation almost 060-20 (trend and plunge); sinistral shear sense of reactivation.

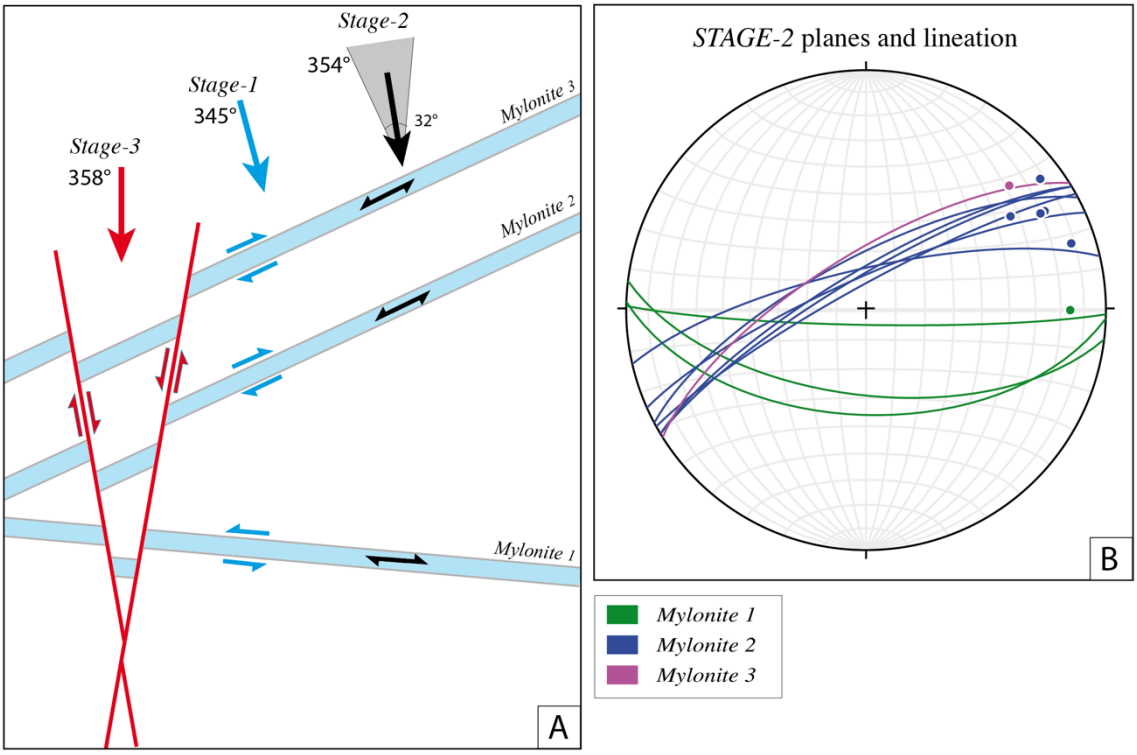

Fig. 10 a) Scheme of the map orientation of the Stage-1-3 reporting the kinematics of the different deformation stages and the associated shortening directions (blue: Stage-1 deformation; black: Stage-2 deformation; red: Stage-3 deformation). For Stage-2 deformation, both the possible range of orientation of the shortening direction (gray wedge) and the calculated shortening direction based on the slip tendency analysis (black arrow) are reported. b) stereoplot (Schmidt, Lower hemisphere) with planes and lineations of Stage-2 structures within the Stage-1 Mylonite $_{1\text{-}3}$.

1.3 Structural Surface Maps

Field observations were integrated with a photographic on-ground and drone survey. The drone used is a DJI Phantom 4 Pro with a built-in high-resolution camera. Flights were planned using DJI software (DJI GO4 and DJI GS Pro) and common flight parameters were: (i) flight height 15 m (minimum); (ii) photograph overlap ratio (70%: front; 60%: side). This setting commonly resulted in a photograph resolution of <1cm/pixel. The photograph overlap allowed a good photogrammetric analysis for the reconstruction of the

3D outcrop model. Elaboration of the photographs were made using the AgiSoft software. From the calculated 3D models, high resolution, geo-referenced (GEOTIFF format) azimuthal ortho-photographs were obtained for map drawing in ArcGis (Fig. 2, 4). These drone-based maps were integrated with higher resolution maps of selected small areas based on photographs taken directly on-ground (Fig. 6, 8, 9).

1.4 Paleostress inversion and Slip Tendency analysis

The maximum shortening direction (σ_1) associated with *Stage-2* shearing was calculated with the Win_Tensor software (Delvaux and Sperner, 2003; Delvaux, 2011) from the orientation of shear zone planes and lineations, and from the shear zone kinematics. From the calculated principal stress axes, we estimated the friction coefficient for the reactivated surface operating a normalized slip-tendency analysis (Lisle and Srivastava 2004). We followed the approach of *Traforti et al.* (2018). The normalized slip-tendency has been calculated directly for every plane with Win_Tensor. The value for the normalize slip-tendency is expressed as:

$$NTs = \frac{Ts}{Max(Ts)} = \frac{\tau}{\sigma_n} * \frac{1}{\mu_0}$$

where $Ts = \tau/\sigma_n$ (where τ is the shear stress and σ_n is the normal stress) is the slip-tendency defined by *Morris* (1996), and *Max(Ts)* is the maximum value for slip-tendency, reached when $\tau/\sigma_n = \mu_0$ (μ_0 is the average friction coefficient for pristine crustal rock).
Considering that during *Stage-2* deformation new ideally oriented, Andersonian shear and extensional fractures did not develop (as in contrast occurred during the *Stage-3* deformation) and that the slip exploited the pre-existing *Stage-1* foliation, we can constrain an upper bound for the value of the friction coefficient on the planes. The value will be:

$$\mu_f < NTs * \mu_0$$

For μ_0 a value of 0.7 was used (Traforti, 2018).

1.4.1 Shortening direction

The result of the paleostress inversion is shown in the plot of Fig. 11 and indicates a shortening direction of 354°. The reduced stress tensor obtained is not a pure strike-slip tensor but is compatible with a certain percentage of inverse movement. The calculated

Stage-2 shortening direction is close to the shortening directions estimated for *Stage-1* and *Stage-3*. The *Stage-2* shortening direction is oriented at a high angle with respect to the reactivated surfaces, meaning that the resolved shear stress on the slip planes was not very high or, in other words, that the friction coefficient on the planes was quite low.

1.4.2 Friction coefficient

Normalized slip-tendency values range between 0.45 and 0.17 (Fig. 11), due to the high angle between σ_1 and the reactivated *Stage-1* foliation. These values indicate that the resolved shear stress on the reactivated foliation was very small with respect to the resolved shear stress that could have acted on newly developed planes. The maximum expected frictional coefficient μ_f during *Stage-2* reactivation ranges between 0.31 and 0.12.

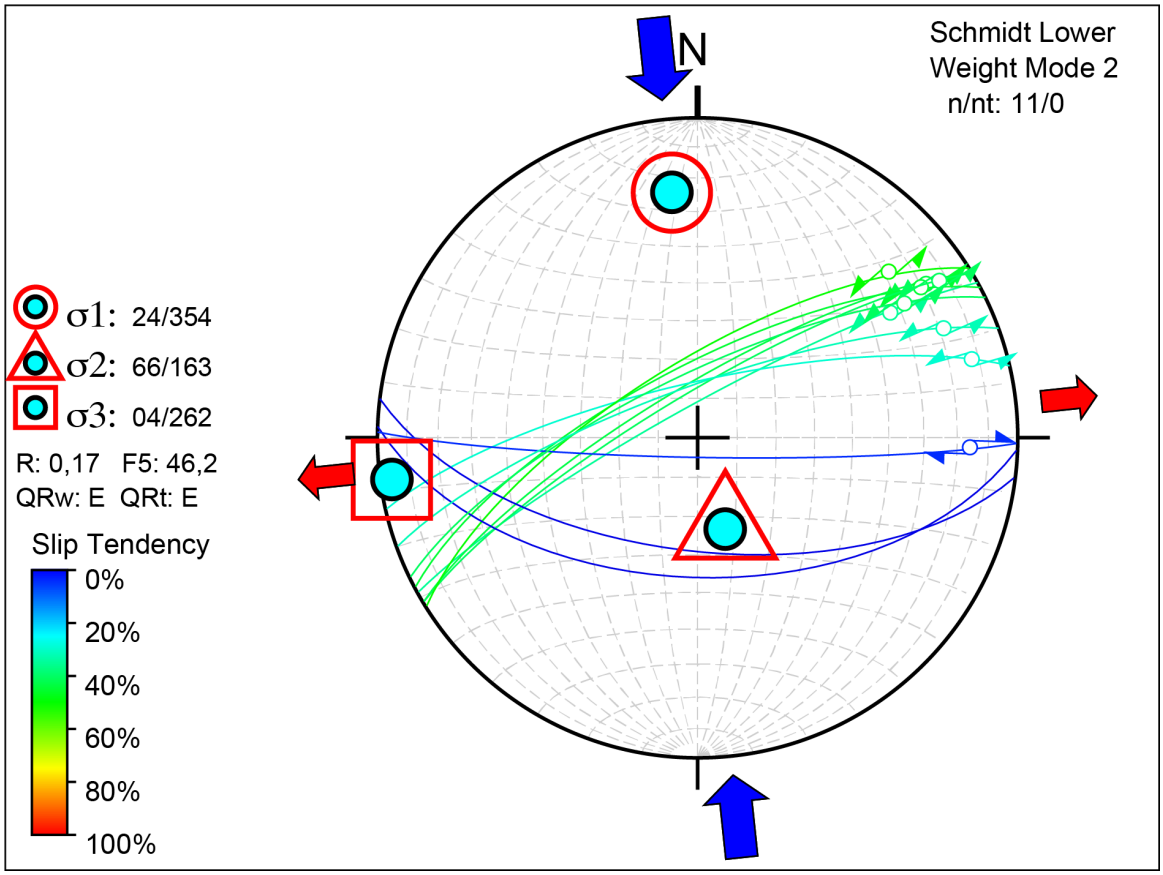

Fig. 11 Stereoplot with the principal stress axes and Stage-2 planes color-coded as a function of their normalized slip tendency (legend in the lower left corner)

2. Petrography and optical observations

A series of oriented samples of *Stage-2* mylonites and pseudotachylytes were taken with the aim of establishing from the microstructural, petrographic and textural analysis: (i) the kinematics of *Stage-2* mylonites; (ii) the metamorphic conditions of formation of *Stage-2* deformation; and (iii) the relationships between *Stage-2* mylonites and pseudotachylytes occurring along the same structural planes.

The collected samples were investigated by optical and scanning electron microscopy for the kinematic and petrographic analysis. The results are described in the following sections. The microstructural analysis was also addressed at selecting the areas for the EBSD analysis described in detail in section 3.

2.1 Sample preparation and Methodology

The selected samples were cut orthogonal to the foliation (XY plane in the shear zone reference system, with X oriented parallel to the lineation) and parallel to the lineation. The thin sections were both polished (ready for SEM investigation) and glass-covered (for simple optical observations). All the sections have the standard thickness of 30 μm.

Optical observations were performed with a common petrographic microscope in transmitted light. The microphotographs were taken with an AxioCam MR5 camera. The use of a first-order red (gypsum plate) was useful to identify the presence of a *c*-axis CPO in quartz aggregates.

SEM investigations were performed with a CamScan MX3000 scanning electron microscope, equipped with a tungsten filament, at the Department of Geoscience of the University of Padova. Working condition were: 25 kV accelerating current, and 15 mm working distance. Images were acquired in BSE (back-scattered electron mode). In order to better identify mineral phases and to qualitatively evaluate their composition, some EDS analyses were performed. For the SEM observations the thin sections were coated with a 10 nm thick carbon layer.

All the sections have been studied under the petrographic microscope. SEM investigations were performed on the two sections 15-124-B1 (mylonite) and 18-182 (pseudotachylyte).

2.2 *Stage-1* mylonite

The *Stage-1* mylonite (Fig. 12a, b) mainly consists of quartz, plagioclase, biotite, muscovite, and minor epidote and garnet. *Stage-1* deformation of quartz at amphibolite facies conditions of around 550 °C ((Hoernes and Friedrichsen, 1974; Friedrichsen and Morteani, 1979) resulted in a coarse (mm) grainsize and lobate grain shapes during grain boundary migration recrystallization. Garnets occur as scattered small euhedral crystals. At this stage of deformation the rock developed a foliation, with a spacing of a few millimeters, defined by alignments of recrystallized biotite and smaller muscovite. Biotite crystals, discordant with the foliation (Fig. 12a), are remnants of the magmatic biotite. Epidote is commonly observed in small crystals along the foliation planes. An incipient S-C foliation is locally developed. A more detailed description of the *Stage-1* microstructures and petrography can be found in Mancktelow and Pennacchioni (2005) and Leydier et al. (2019).

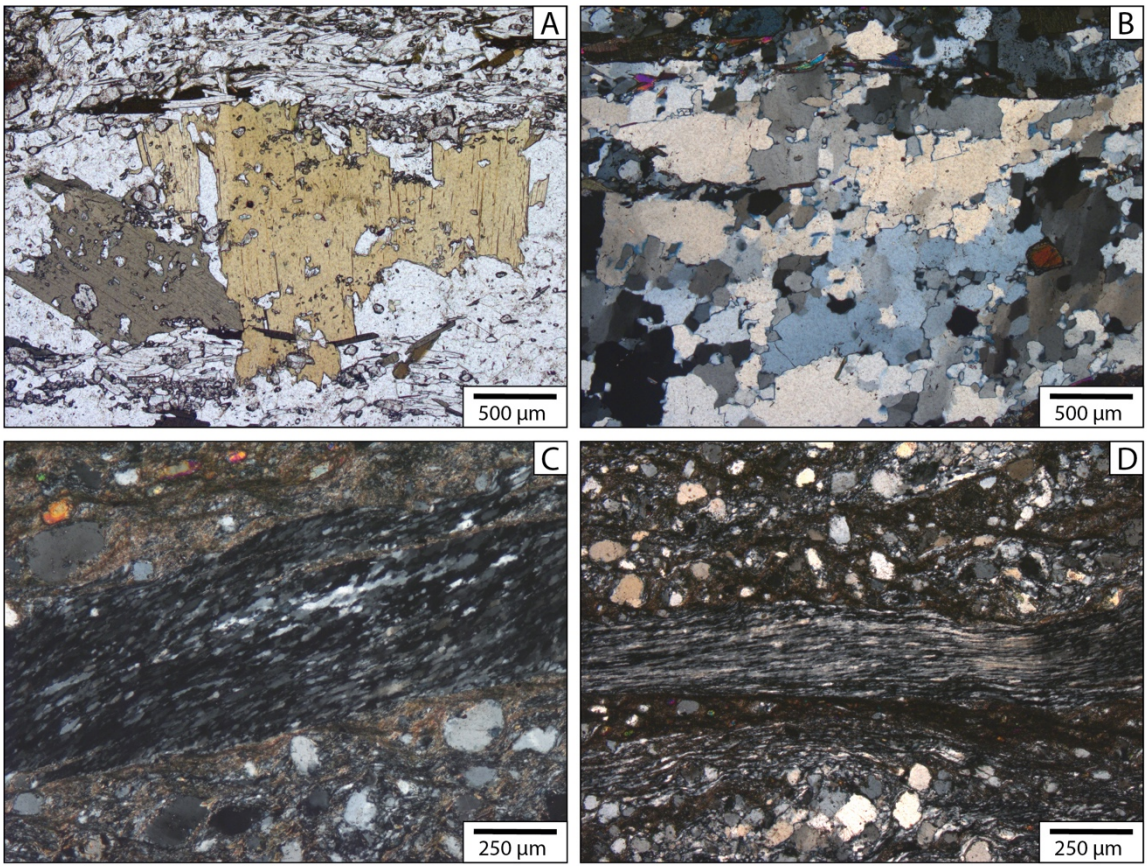

Fig. 12 a) host rock with stable quartz, feldspars, biotite muscovite and epidote; the foliation is marked by small lamellae of muscovite and by trails of small crystals of epidote; b) Stage-1 quartz in equigranular crystals; in the upper part a weak foliation is defined by the orientation of biotite and muscovite; c) ribbon of quartz showing an initial phase of the Stage-2 recrystallization; d) ribbon of quartz with an higher degree of recrystallization (smaller grainsize)

2.3 *Stage-2* mylonite

The *Stage-2* deformation exploited the previous *Stage-1* mylonitic foliation and is localized to thin (commonly around a few millimeters wide) horizons, while most of the remaining precursor *Stage-1* fabric is preserved. Around the main exploited foliation plane, some others secondary planes, both distinct or partially linked to the main one, show signs of reactivation.

The most remarkable petrographic change during *Stage-2* deformation, when compared with *Stage-1* metamorphic assemblage, is the absence of garnet in the synkinematic mineral assemblage. Garnet occurs only as porphyroclast (Fig. 13 d) within *Stage-2* mylonite and is never preserved in pseudotachylyte. Epidote is stable both in the *Stage-1* and in the *Stage-2* mylonites, but in the latter case it commonly shows a relatively Fe-poor core with respect to the rim (in BSE the core is of a darker gray) (Fig. 13 f). Epidote commonly forms porphyroclasts in the *Stage-2* mylonite, wrapped around by the biotite foliation.

Biotite is present in two generations of a slightly different composition (evidenced by different grey tones in BSE), probably reflecting two different stages of crystallization (likely referable to *Stage-1* and the *Stage-2* stages). Near the reactivated planes, biotite is kinked. These structures, typically associated with brittle rupture, are observable around both the mylonitic and the brittle reactivations.

The stable plagioclase in *Stage-2* mylonite has an oligoclase composition (around Ab_{75}) and exhibits evidence of dynamic recrystallization and associated grain-size reduction.

Considering the structures of the mylonitic reactivation, a transition from the precursor fabric to the most deformed *Stage-2* shear planes is observed. Moving towards *Stage-2* high strain zones, quartz first shows as an incipient recrystallization with elongated new grain defining a shape preferred orientation. With increasing strain the grainsize progressively decreased and locally developed higher aspect ratio grains typically organized into elongated ribbons (Fig. 12 c, d). These ribbons of remarkable dimensions relatively to the other recrystallized quartz aggregates show a marked crystallographic preferred orientation (evincible in cross-polarized light with the use of a gypsum plate). In the final stages of mylonitization quartz was affected by pervasive recrystallization to a very small grain-size (a few micrometers), relegated to tiny ribbon-like domains embedded by the mylonite (Fig. 13 a) or close to the exploited foliation. Two of these domains (Fig. 16) have been selected for in-depth EBSD analysis (see section 3).

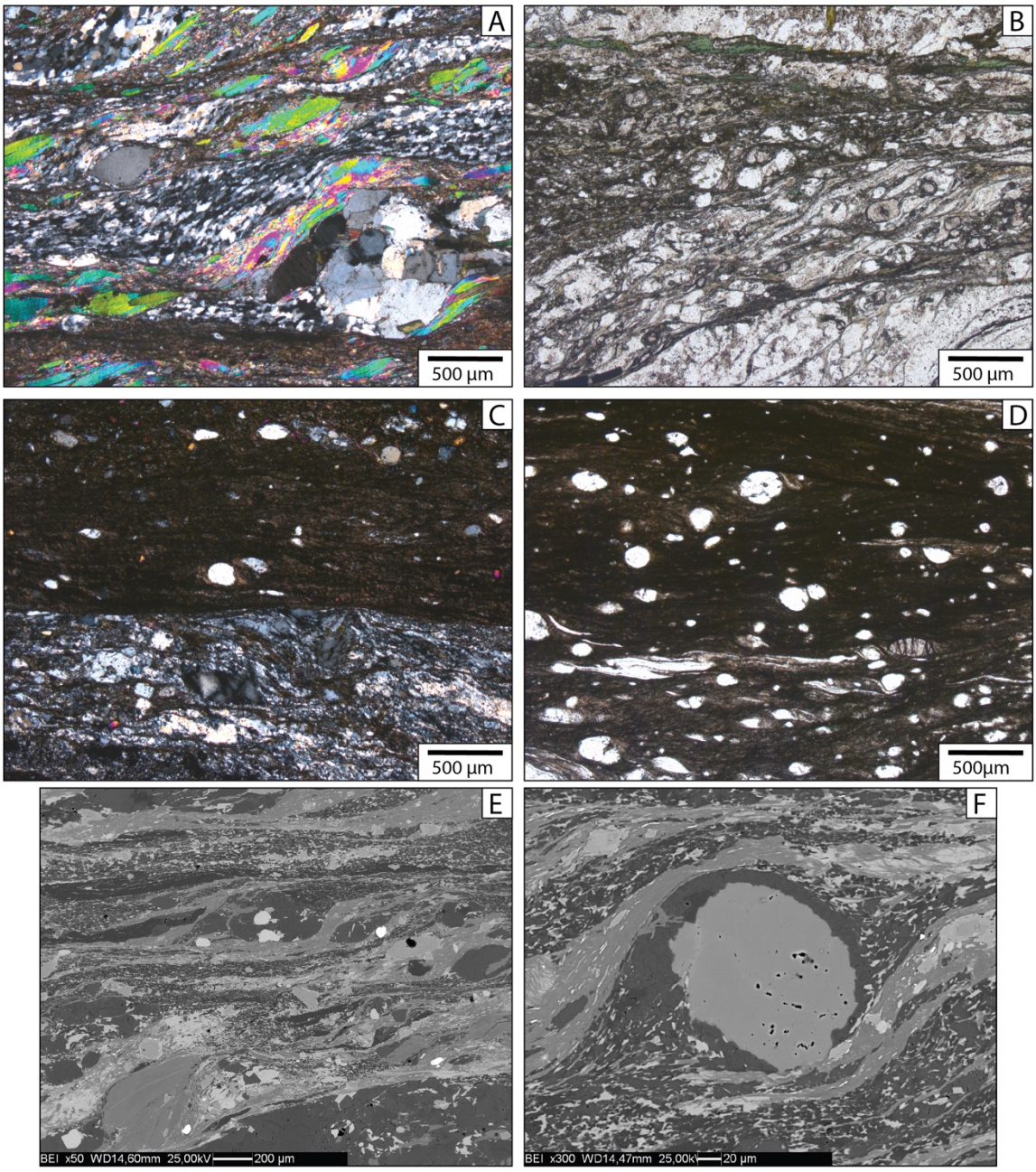

Fig. 13 Optical and BSE images of the Stage-2 mylonite: a) portion of quartz with an intense recrystallization, bounded by phyllosilicate lamellae and by the mylonitic matrix; b) mylonite exploiting the pristine foliation; c) ultramylonite with an extremely fine grained matrix and a sharp boundaries with the rest of the rock which also shows evidence of intense Stage-2 deformation; d) mylonite with rounded porphyroclasts and a relict porphyroclast of garnet; e) Highly foliated Stage-2 mylonite; f) porphyroclast of plagioclase crowned by the growth of quartz and by the biotite of the foliation

2.5 *Stage-2* Pseudotachylyte

Under the petrographic microscope and plane-parallel light, pseudotachylytes appear as a brown-colored irresolvable matrix (Fig 14). In some cases, patches of the matrix are birefringent under crossed polarizers owing to recrystallization to an ultrafine aggregate of oriented phyllosilicates. Typically, pseudotachylyte fault veins have sharp boundaries with *Stage-2* mylonites and locally small injections veins depart from the fault vein intruding the mylonitic foliation (Fig. 14 b, c). Pseudotachylyte is commonly associated with a very fine grained cataclasite, which can exhibit a foliation (Fig. 4a), but pseudotachylytes are not overprinted by a ductile (crystal plastic) deformation. Pseudotachylytes are present both in direct contact with the pristine host rock or with the *Stage-2* mylonites, confirming their mutual relation as observed on the field. The injection veins intruding and crosscutting the *Stage-2* mylonitic foliation points toward a sequential development with the mylonite forming before pseudotachylyte, as evidenced also from the absence of a foliation in the pseudotachylyte.

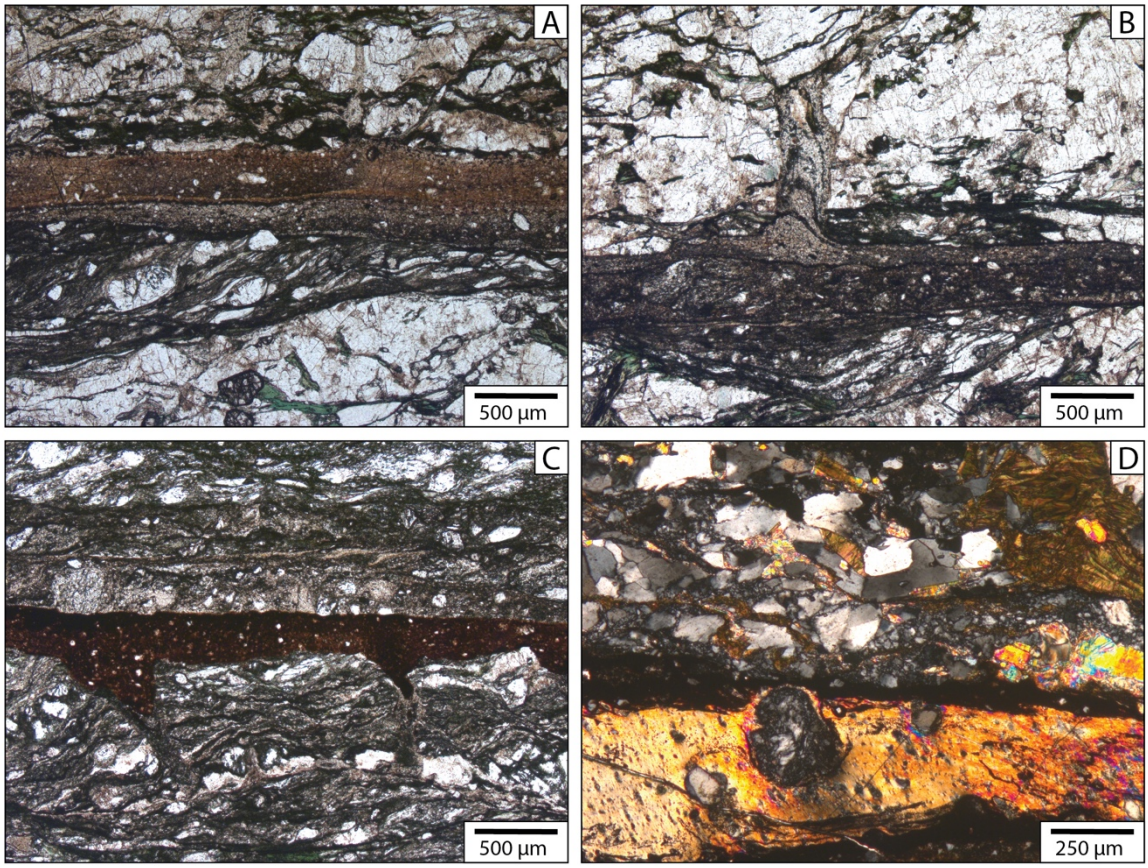

Fig. 14 optical images of Stage-2 pseudotachylyte: a) pseudotachylyte cutting a mylonite; b, c) pseudotachylyte with small injection veins; d) big porphyroclast of plagioclase in a melt pocket birefringent due to the incipient recrystallization of phyllosilicates

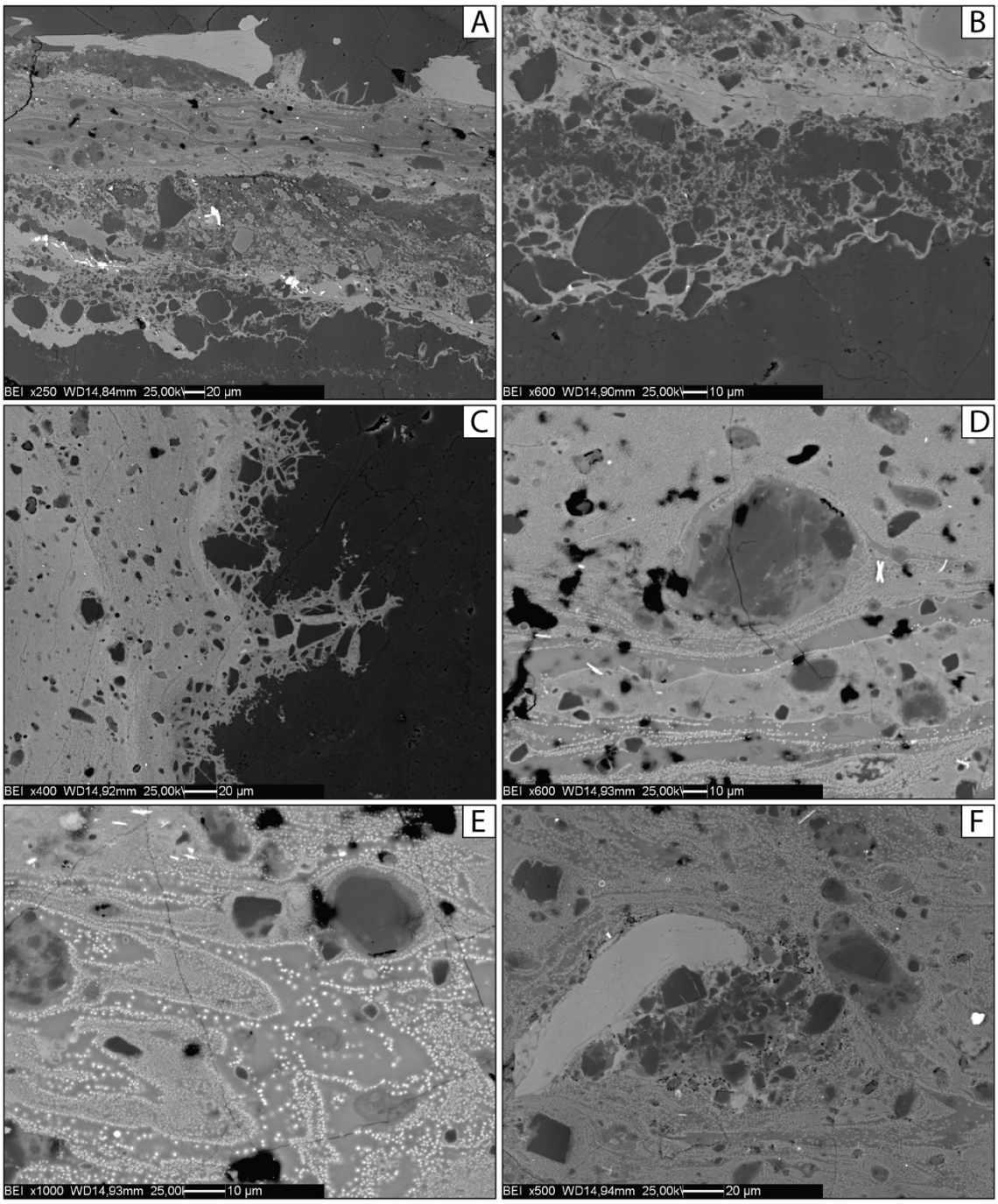

Fig. 15 BSE images of the Stage-2 pseudotachylyte: a) pseudotachylyte associated with a foliated cataclasite; a small injection veins are present; b) detail of the cataclasite; c) pseudotachylyte border defined by the presence of small fragment of crushed quartz; d, e) clasts and trails of microlites defining flow structures inside a pseudotachylyte; f) clast of biotite with crushed quartz and plagioclase

On closer inspection, the margins of pseudotachylyte are decorated by angular fragments of quartz (Fig. 15c) likely formed during thermal shock-induced fragmentation during the seismic event (Papa et al., 2018). Angular clasts of quartz, feldspars, epidote and, in rare cases, biotite are also present inside the pseudotachylyte, with plagioclase clasts commonly

showing melted margins (Fig. 15 d, e, f). Clasts are embedded in an extremely fine matrix, unresolvable even under the SEM at high magnification. In a few cases these clasts, remnants of the host rock incorporated by the pseudotachylyte, are of noticeable dimensions (fig. 14 d), but usually they are not more than some tens of micrometers in diameter. At the highest magnifications, microlites (mainly of oxides) are visible inside the pseudotachylyte. Some of them are elongated, with a cross-like or dendritic shape, and may be arranged in trails defining flow structures (Fig 15 d, e). The presence of some droplets of sulfides confirms the melt origin of the pseudotachylyte (Magloughlin, 2005).

At the selvages of the pseudotachylyte the host rock, at the very contact (within a few 10s microns) with the vein, shows domains with both quartz and plagioclase with an extreme grainsize reduction (Fig. 14 d), similarly to the most intensely recrystallized portions of quartz in the *Stage-2* mylonites. An organized extinction observable under the microscope (cross-polarizers) suggests that the intense reduction in grainsize was determined by a process of dynamic recrystallization which can be attributed to a thermal transient due to frictional melting (Bestmann et al., 2012).

3. EBSD analysis of *stage-2* deformed quartz

EBSD analysis is a powerful tool to obtain information about the microstructures and CPO (Crystallographic preferred orientation) of mineral aggregates (Prior et al., 2009). This analytical technique can be used to estimate parameters such as the active slip systems at the time of the deformation, the size of subgrains and new recrystallized grains, the orientation of misorientation axes of low and high angle boundaries. These data provide constraints about the deformation mechanisms and ambient conditions of deformation.
The EBSD analysis of quartz aggregates in *Stage-2* mylonites has been a main task of my thesis. This analysis aimed at determining the deformation mechanisms in the most evolved (strained) mylonites, geometrically associated with pseudotachylytes and at estimating the differential stress during mylonitization based on paleopiezometry.

The investigation was focused on quartz, since it is the best constrained mineral in terms of mechanical behavior during crystal-plastic flow, both from experiments and from field data (Bestmann and Pennacchioni 2015; Hirth and Tullis, 1992; Stipp et al., 2002; Stipp and Tullis 2003), as well as one the most common minerals in rocks of the continental crust. Quartz is usually considered to control the rheological behavior of the crust (Ranalli, 1995) and, given its symmetry and simple chemical composition, it is the best candidate for EBSD microstructural investigation.

3.1 Sample preparation and methodology

The EBSD analysis was performed on sample 15-124-B2, selected by optical investigation as the sample showing the highest degree of grain size refinement in *Stage-2* mylonites. Figure 16 shows a cross-polarized scan of the studied thin section.

The thin section was polished with a colloidal silica suspension (SITON) for several hours. This procedure removes the surface damaging of the thin section, induced by the standard polishing preparation, allowing the electron backscattered diffraction analysis. The final preparation of the sample consists in a carbon coating (approximately 3.8 nm thick). This procedure is not required for EBSD analysis, but the initial plan was to perform also cathodoluminescence investigation on the same areas and, being the coating required for CL, we used this thickness of coating in order to be able to perform both the analyses

without re-polishing of the surface. Unfortunately, the quality of CL images wasn't good enough to give significant information and so they are not presented here.

The EBSD investigation was performed at the Scientific Center for Optical and Electronic Microscopy (ScopeM) of ETH Zurich under the supervision of Luiz Morales. Data were acquired using a FEI Quanta 200F equipped with a field emission gun and an EDAX Hikari detector for EBSD. Working conditions for the acquisition were: 20 kV, 7nA and working distance of 15-18 mm with a tilt of the sample holder of 70°. The used spot sizes were 0.2 0.5 and 1 µm.

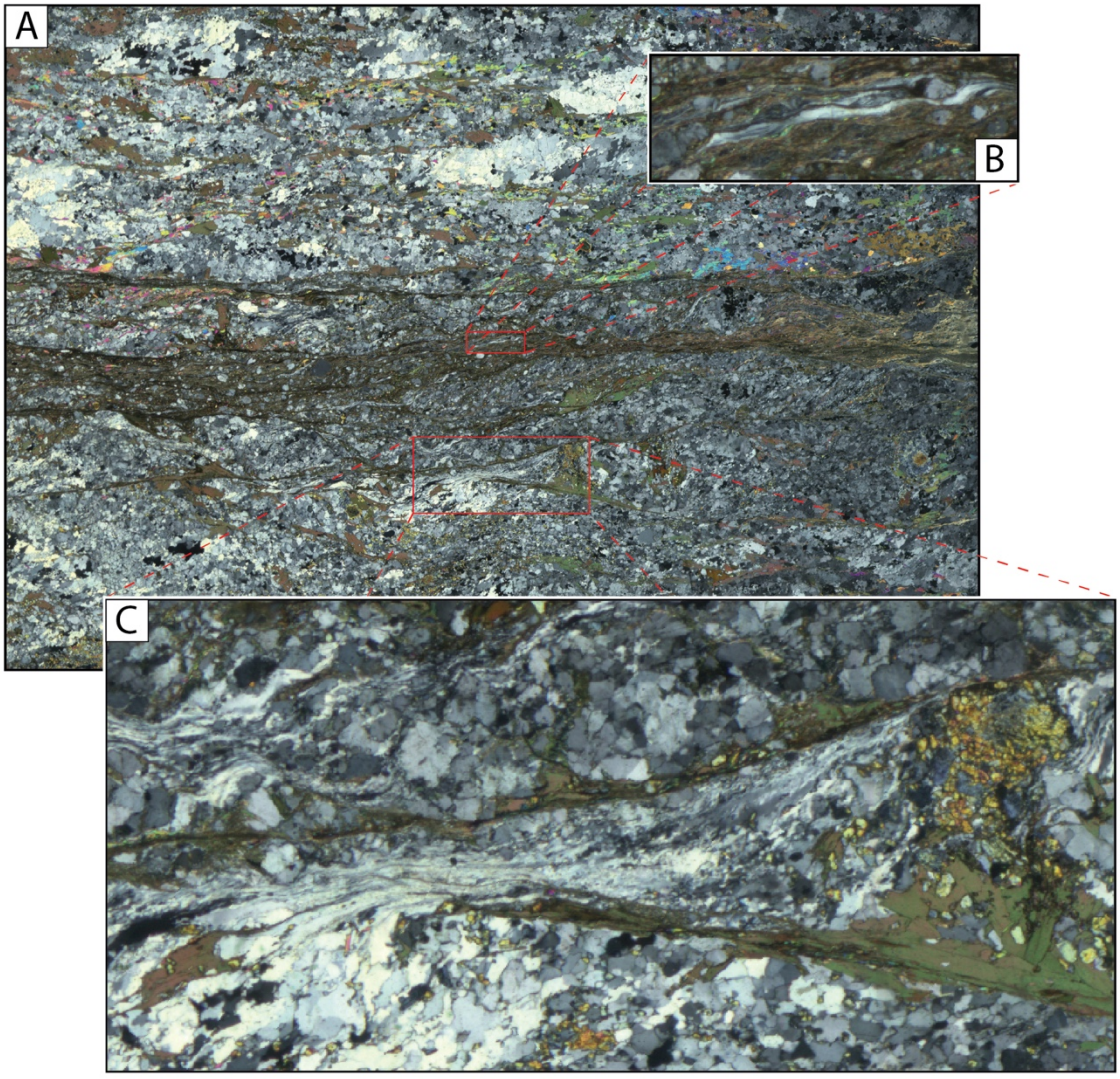

Fig. 16 Scan with cross-polarizers of the thin section 15-124-B2 object of the EBSD investigation, with a focus on the two mapped areas: b) Map 1 and c) Map 2

3.2 Data acquisition and processing

Two small portions of the thin section were identified for EBSD analysis. Two maps were collected with a step size of 0.5 μm (map 1) and 1 μm (map 2). A third map, comprising a little portion of map 2, was acquired with a step size of 0.2 μm for a better estimate of the grain size. The acquisition was done with a hexagonal pixel in order to obtain better looking grains during processing. To speed up the acquisition time, only quartz (trigonal 32 symmetry) was considered, reaching a measurement velocity of up to 70 fps. The other phases were added during the reprocessing of the maps.

The raw data were preliminary cleaned with OIM software. The procedure consists in calculation of grains and filling of empty pixels with an interpolation. The maps were then saved in the ANG file format (a format that can be read even with a simple text editor).
Subsequent elaboration and analysis of the maps were carried out with MTEX, an open source Matlab-based software by Ralf Hielscher (Bachmann et al., 2011; Mainprice et al., 2015). The original maps were divided into different subsets dividing the regions of interest. This procedure was particularly useful to isolate quartz domains showing different degrees of recrystallization.

Since the study was focused on quartz, all the other mineral phases were deleted, reducing the calculation time. All the points with a confidence index lower than 0.1 were discarded (set to "not indexed"), since point with lower values were not measured sufficiently well (probably they weren't quartz at all). After a preliminary calculation of the grains, the included not-indexed holes below a certain size were set to "empty"; then the grains were calculated again making the software to automatically fill the empty holes inside grains. Grains with a number of pixels lower than 10 (6 for the map 2) were deleted to be confident enough that the calculated grains were real ones. For the calculation of grains, a critical misorientation of 10° has been considered (Shigematsu et al., 2006).
In order to disregard the Dauphinè twinning (a rotation of 60° along c axis) as a grain boundary, the crystal symmetry of quartz was changed to hexagonal (6mm), then grains were calculated, and finally the symmetry was restored to the original one. This procedure permits to discard the effect of twinning preserving all the other data (Kilian and Heilbronner, 2017).
The distinction between recrystallized grains and relict grains was carried out following the procedure proposed by *Cross 2017* – the GOS (grain orientation spread, an index for the

internal deformation of crystals), calculated for each grain, was used as the discriminating parameter between the two populations of relict and recrystallized grains. Using a trade-off curve (Matlab code from the supplementary material of *Cross* 2017) with cumulative number of grains versus GOS the threshold value was calculated for each subset. The grain size is given as equivalent diameter. The value considered more realistic in order to obtain an estimate of the average grain size for a population of grains, even if more affected by the bigger grains, is the square mean roots (Cross 2017, Stipp and Tullis 2003).
The contoured pole figures were obtained from an orientation distribution function considering one orientation per grain, calculated with a *de la Vallée-Poussin* kernel with an halfwidth of 10°. All the pole figures are equal area and antipodal. The inverse pole figures for misorientation axis have been calculated at fixed angular intervals (as well as for the misorientation axis distribution in sample coordinates). The misorientation angle distributions are always plotted together with a random distribution (Montecarlo approach, calculated directly with MTEX) and the uncorrelated distribution.

3.3 Results

In the following sections a description of the analyzed quartz domains is reported. For every considered subset, the pole figures and the orientations of misorientations axes are presented. Pole figures and misorientation axis distributions in crystal and sample coordinates are reported in Fig. 24 and 25; the misorientation angle distribution is shown in Fig. 23.

3.3.1 Map 1

This map (Fig. 17) comprises two ribbons of fine grained aggregates of quartz bounded by fine grained biotite layers. These quartz aggregates are situated at the border of a foliation surface which have been reactivated determining the fine recrystallization of the quartz. The foliation pattern defines a composite S-C foliation, marked by the elongation of biotite and other ribbons of quartz. The two ribbons have been analyzed separately.

3.3.1.1 Ribbon 1

This quartz ribbon is largely recrystallized at the upper and lower border, while the inner portion consist of few larger (as large as over 1 mm), elongated grains. These larger grains show a complex internal pattern of subgrains of a dimension comparable to the

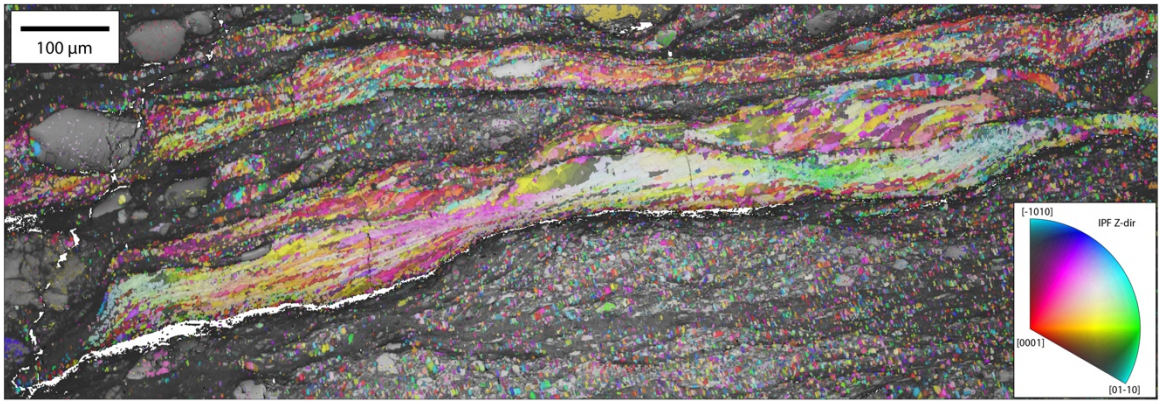

Fig. 14 Orientation contrast map of Map 1 comprising the two ribbons, color coded according to the inverse pole figure in the bottom right corner.

recrystallized grains. The distribution of new grains and the larger relict grains suggests that initially the ribbon was made of only a few large grains. (Fig. 18)

The pole figure for the *c*-axis shows a single maximum in the rhomb position. The inverse pole figure for misorientation axes has a maximum in the *c*-axis direction; for low misorientation angles this maximum is less marked and there is a slight concentration toward the rhomb position. In sample coordinates the misorientation axis distribution is concentrated between the Y and Z direction (and shifts toward Z at higher angles) (Fig. 24 a). For correlated distribution, the misorientation angles show maxima at angles around 10° and 60°.

3.3.1.2 Ribbon 2

This ribbon is more extensively recrystallized than ribbon 1. The new grains are smaller and show a marked polygonization. In contrast to ribbon 1, very elongated grains are almost absent, which also supports a higher degree of recrystallization of ribbon 2. (Fig. 19)

The *c*-axis pole figure shows a single maximum in the rhomb position. The high angle misorientation axes show a maximum in the *c*-axis position while for low misorientation angles a second maximum appears in the rhomb position. In sample coordinates the misorientation axis distribution defines peripheral maxima at medium and high angles, while for low angle the axis are concentrated between the Y and rhomb directions (Fig. 24 b) The correlated distribution of misorientation angles is defined by a maximum at low angles and one at 60°.

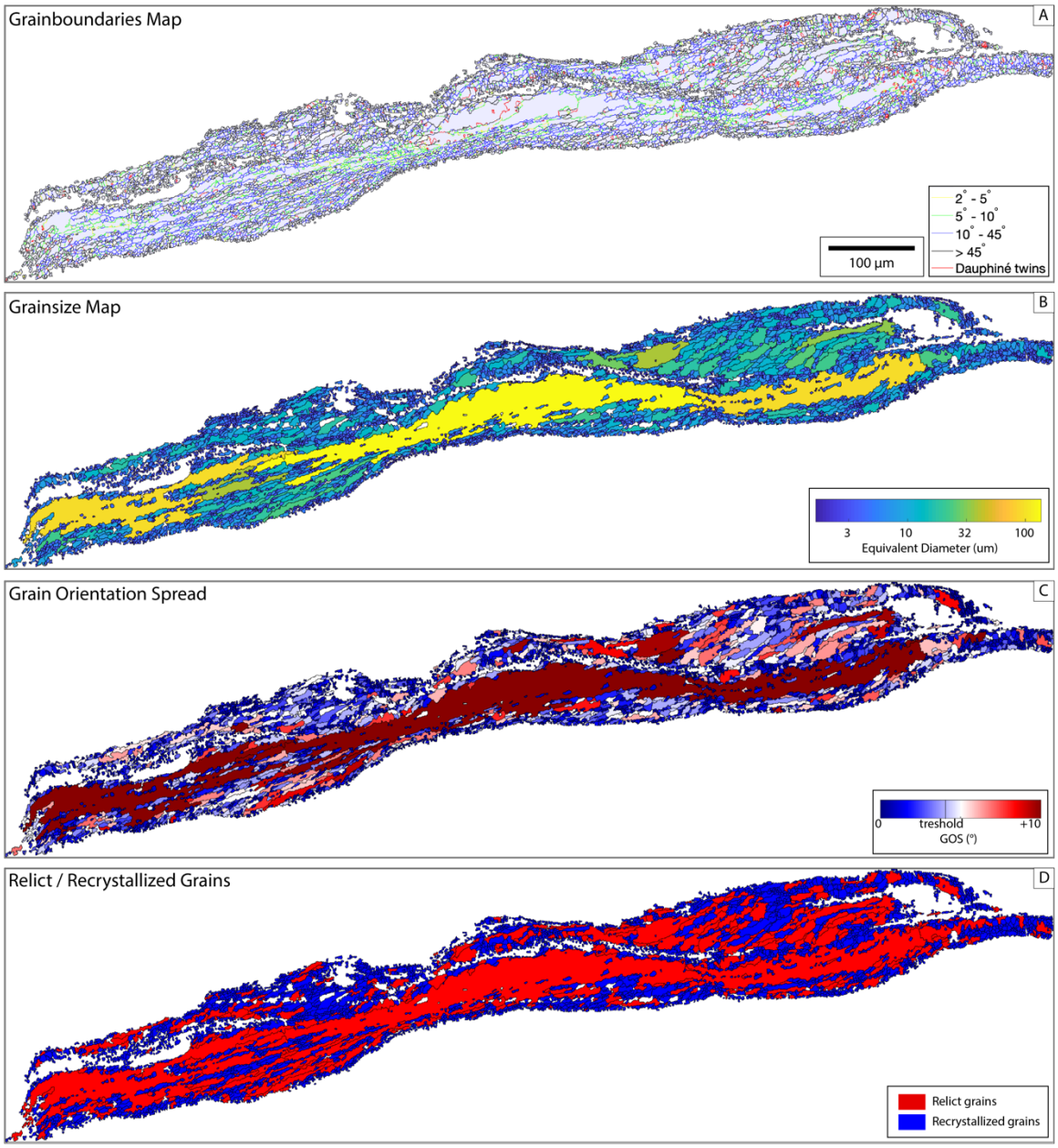

Fig. 18 EBSD map of Ribbon 1: a) map of the misorientation angles, colored according to the legend in the bottom right corner; b) map with grains colored in function of the equivalent diameter; c) map of the GOS, in the legend the GOS value corresponding to the split between recrystallized and relict grains is marked; d) distinction between the two grain populations

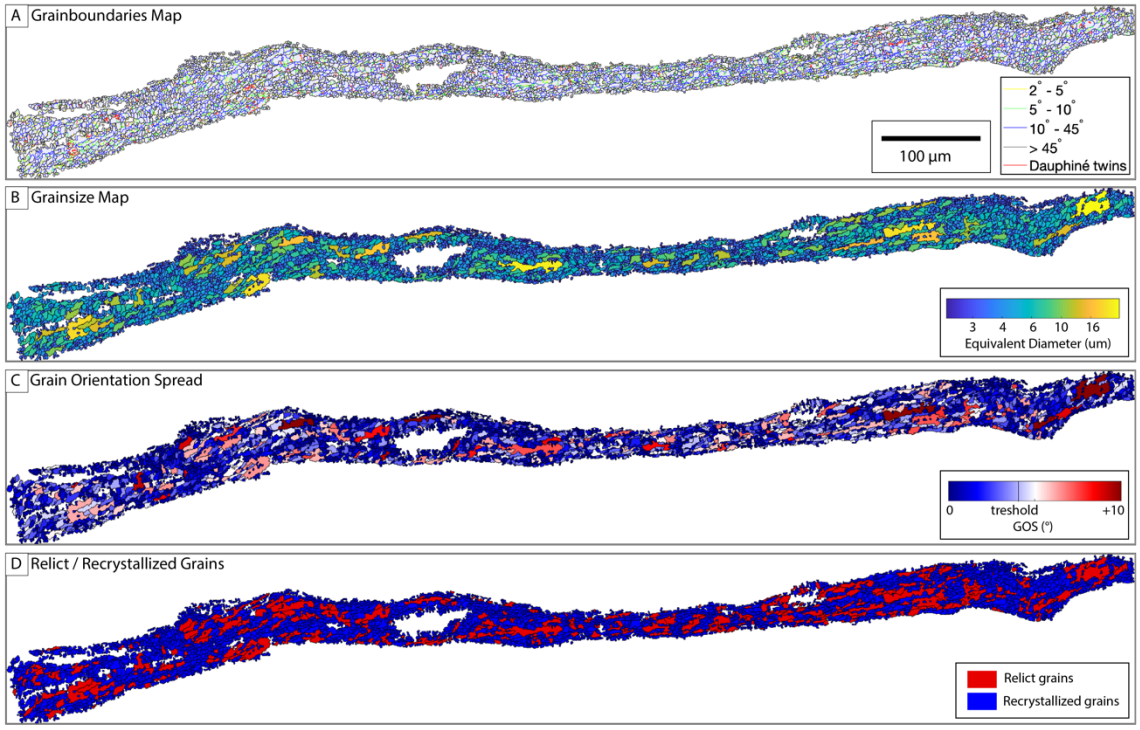

Fig. 19 EBSD map of Ribbon 2: a) map of the misorientation angles, colored according to the legend in the bottom right corner; b) map with grains colored in function of the equivalent diameter; c) map of the GOS, in the legend the GOS value corresponding to the split between recrystallized and relict grains is marked; d) distinction between the two grain populations

3.3.2 Map 2

This area consists of an aggregate of quartz, with some K-feldspar and plagioclase, bounded by two convergent layers of biotite (one marking the foliation and the other probably a secondary surface) where part of the deformation was concentrated. This area was considered because it shows the evolution of microstructures from the earlier, coarse-grained *Stage-1* quartz, to an aggregate of strongly elongated and partially recrystallized grains, and finally to an extensively recrystallized aggregate of polygonal grains. (Fig. 20). Three subsets, corresponding to these 3 different microstructures, have been analyzed separately. A second map with a portion of the extensively recrystallized, polygonal quartz have been acquired using a smaller step size (0.2 µm) in order to better quantify the grain size.

3.3.2.1 Area 1

This area represents an intermediate stage of the reactivation of the *Stage-1* microstructure. Some large *Stage-1* quartz grains are still preserved, but show evidence of the incipient

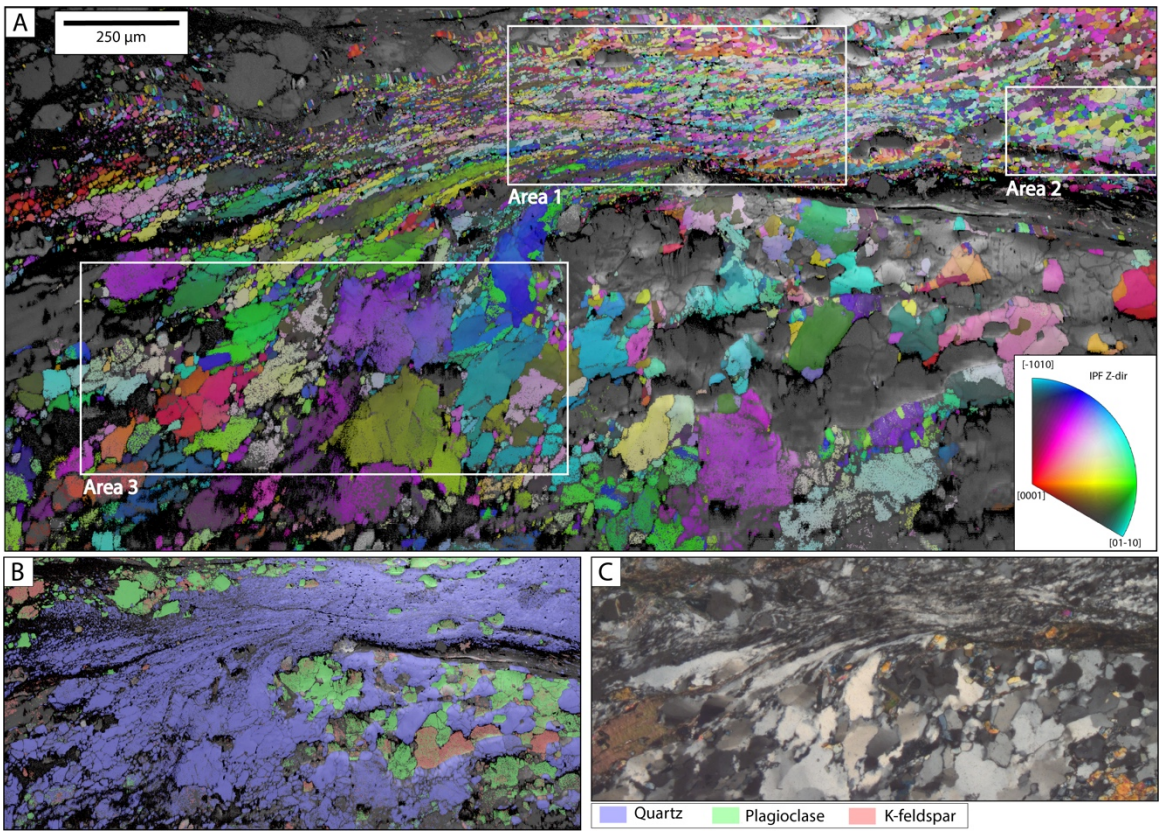

Fig. 20 a) Orientation contrast map of Map 2, color coded according to the inverse pole figure in the bottom right corner; white rectangles are the analyzed subsets; b) phase map, colored according to the legend at the right; c) optical, cross polarized, image of the area

deformation, with abundance of low angle boundaries (subgrains) and the development of new grains. Moving from the bottom left corner to the top right of the domain an increase of the effects of reactivation is evident, with quartz grains progressively more elongated before starting to show a marked polygonization and local recrystallization. A shape preferred orientation of the elongated grains in the direction of deformation is evident (Fig. 21).

In the pole figure, the *c*-axis distribution is defined by maxima in the rhomb position. The misorientation axis distribution in sample coordinates is defined by a maximum in the rhomb position (with a little dispersion toward the secondary rhomb), while at medium and high angle the maxima are in *c*-axis direction. In sample coordinates the misorientation axis are distributed in peripheral positions for medium and high angles, while define a maximum centered between Y and the rhomb direction for low angles (Fig. 25 a). The correlated misorientation angles distribution is defined by a small maximum at low angles and by a marked maximum at 60°.

3.3.2.2 Area 2

This map portion represents the most strongly recrystallized domain. The spread in grainsize is reduced with respect to the area 1, suggesting that recrystallization almost completely obliterated the *Stage-1* features. Unfortunately, due to the small number of grains, the distinction between recrystallization and relict populations is not meaningful (Fig. 22).

In the pole figure the *c*-axis distribution defines a girdle around the rhomb position. The misorientation axis distribution has (i) a maximum in the *c*-axis direction for high angles, (ii) two maxima in the rhomb and in the *a*-direction for medium angles and (iii) a maximum in the secondary rhomb position for low angles. In sample coordinates the misorientation axis distribution is not clear and shows different maxima (Fig. 25 b). The misorientation angle distribution has just a single maximum at 60°. These results are affected by the low number of measured grains of this subset and therefore are not meaningful.

3.3.2.3 Area 3

This area comprises pristine *Stage-1* grains and has been considered only as a comparison with the recrystallized fabric. Towards the top of the subset, quartz grains show incipient evidence of reactivation; anyway, the aggregate can be considered as representative of the *Stage-1* amphibolite-facies deformation stage.

The pole figure of *c*-axis shows a girdle located at the periphery (Fig. 25 c). Analyzing this figure, it should be considered that the sample was cut along the X-Z plane in the the *Stage-2* reference frame.

3.3.2.4 High resolution

This map, acquired after complete elaboration of the map 2, was done with the purpose of better evaluating the recrystallized grain size. A step size of 0.2 μm (the smallest available) was used to be confident that the grain size is evaluated properly since the step size should always be less than a fifth of the average recrystallized grain size (following *Cross 2017*). Pole figures and inverse pole figures were not considered for this map since the area is the same of map2.

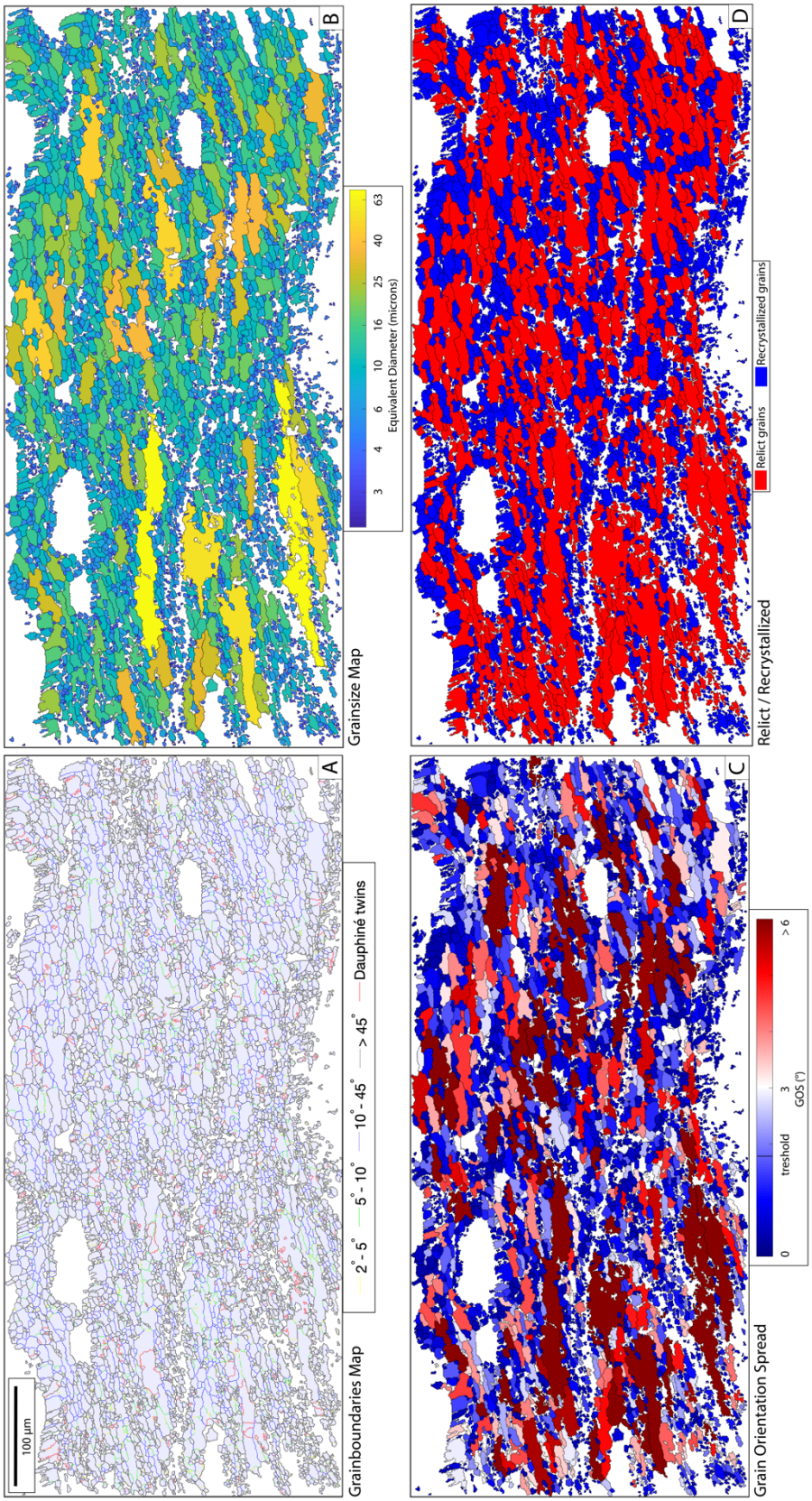

Fig. 21 EBSD map of Area 1: a) map of the misorientation angles, colored according to the legend in the bottom right corner; b) map with grains colored in function of the equivalent diameter; c) map of the GOS, in the legend the GOS value corresponding to the split between recrystallized and relict grains is marked; d) distinction between the two grain populations

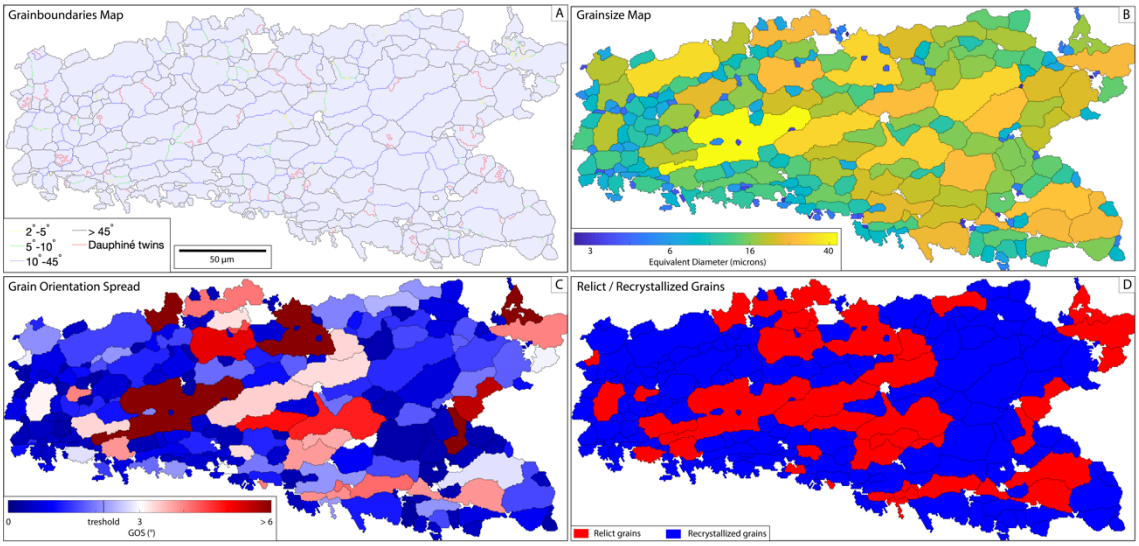

Fig. 22 EBSD map of Area 2: a) map of the misorientation angles, colored according to the legend in the bottom right corner; b) map with grains colored in function of the equivalent diameter; c) map of the GOS, in the legend the GOS value corresponding to the split between recrystallized and relict grains is marked; d) distinction between the two grain populations

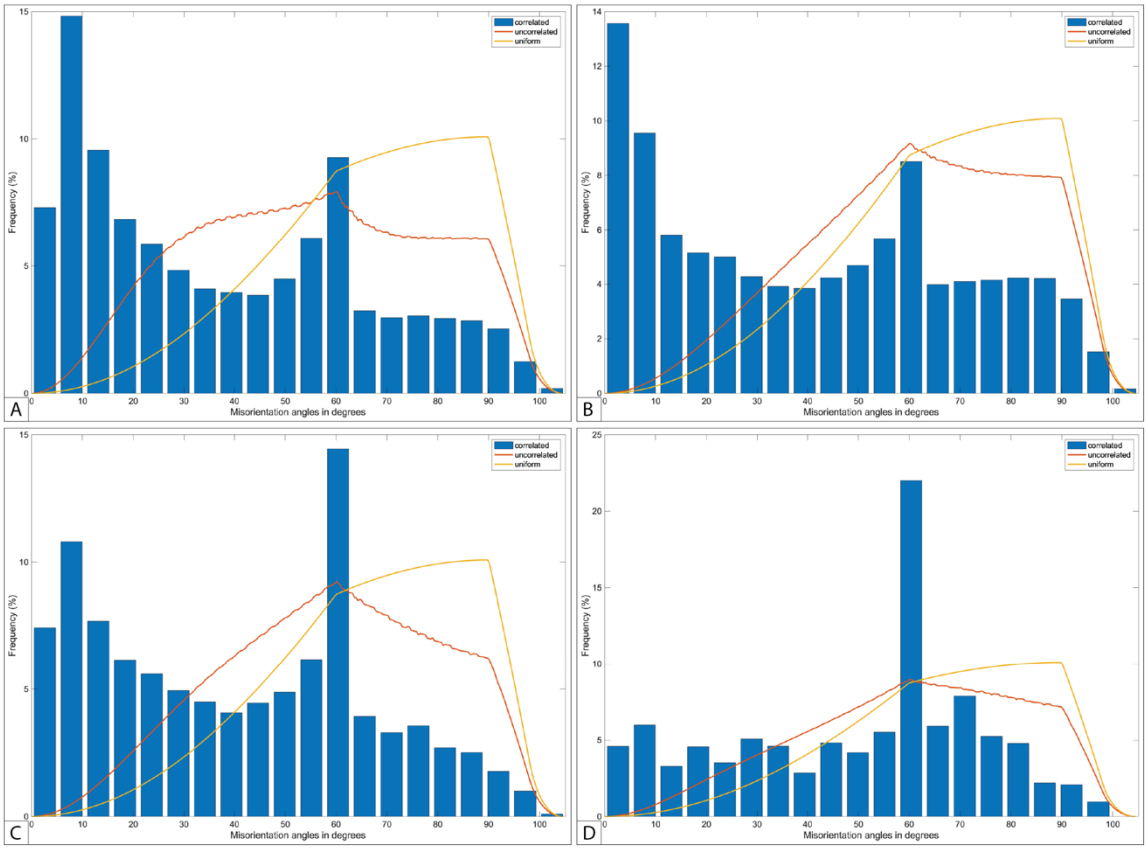

Fig. 23 Misorientation angle distributions for a) Ribbon 1, b) Ribbon 2, c) Area 1, d) Area 2; in every graph also the uncorrelated and uniform distributions are reported

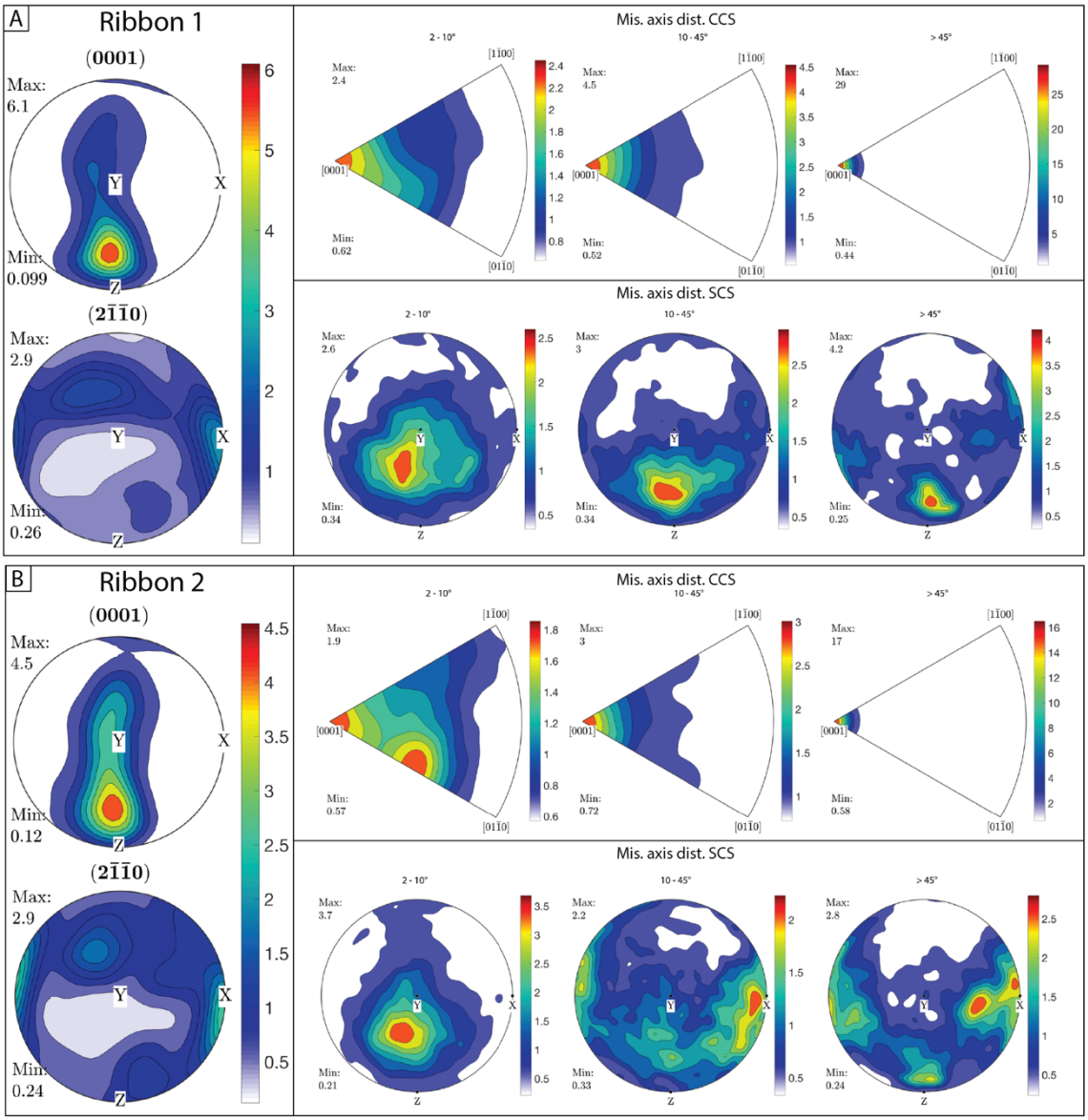

Fig. 24 Pole figure for <c> and <a> directions, misorientation axis distribution in crystal coordinates and sample coordinates, for a) Ribbon 1 and b) Ribbon 2

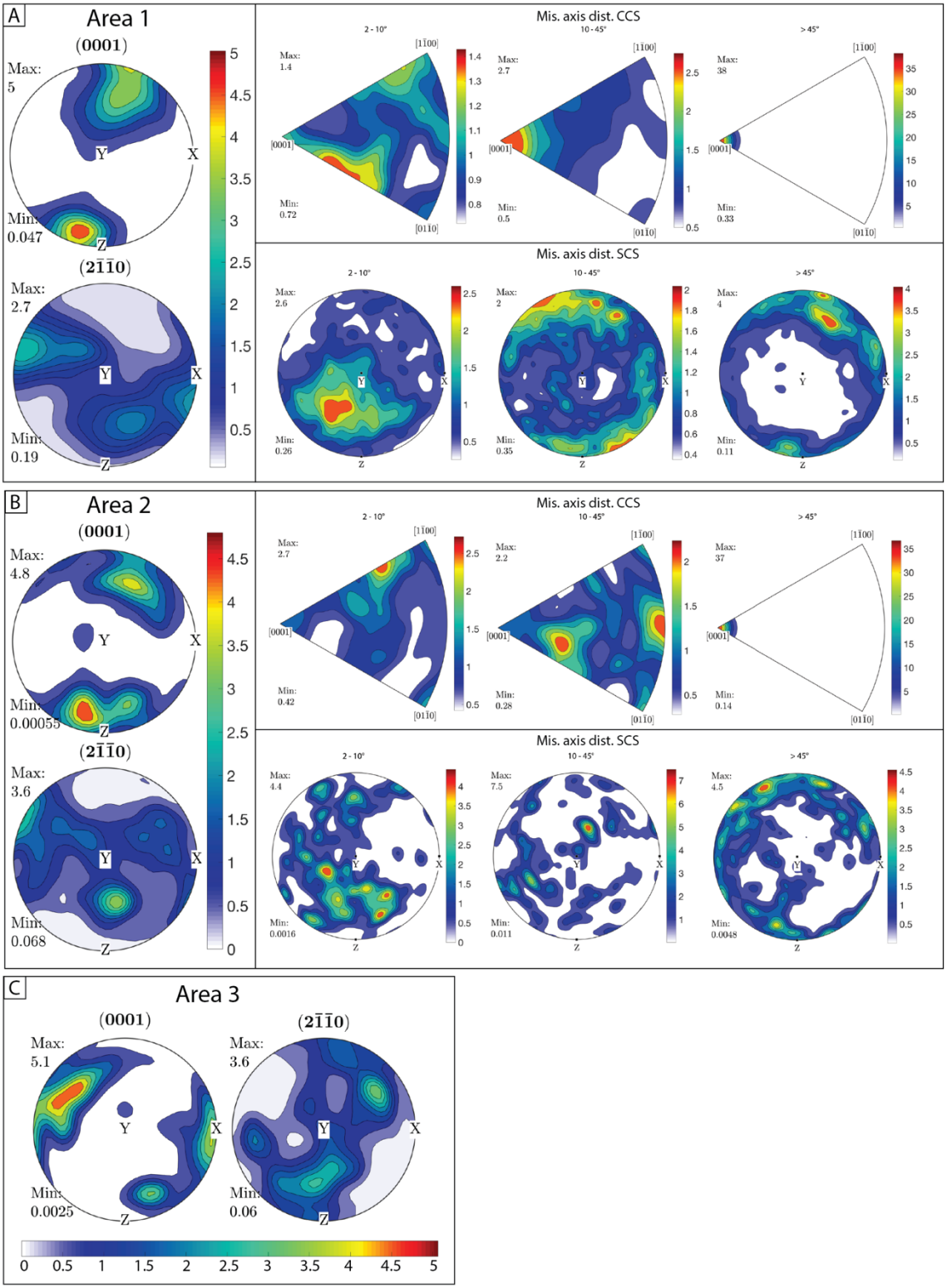

Fig. 25 Pole figures for <c> and <a> directions, misorientation axis distribution in crystal coordinates and sample coordinates, for a) Area 1 and b) Area 2; c) pole figures of Area 3

3.3.3 Grain size of the recrystallized quartz grains

The average grain size of recrystallization was calculated for each subset. In all the maps the efficiency of the GOS-based threshold can be appreciated: the grain with the highest GOS correspond to grains clustered with subgrains while the recrystallized grains appear almost free of subgrains. In some cases, the attribution of quite elongated grains to the recrystallized population can look ambiguous ,but being these grains free of subgrains they can effectively correspond to new grains.

For the map 1 recrystallized grain sizes are 3.8 ± 1.9 and 3.3 ± 1.3 μm (RMS) for ribbon 1 and ribbon 2, respectively. The grain size values calculated as a simple mean of all the grains are 3.3 and 3, respectively.

For the map 2 the calculated grain size is 5.7 ± 2.7 μm (RMS) and, when calculated as simple mean, is 5.1 μm. These values are affected by the spot size used for the measurements, too high for a proper evaluation of the grain size. Area 2 gives relatively high results (11.3 ± 6 and 9.7) but, due to the small number of grains considered, is not a reliable value. Area 3 was not considered because it is formed mostly by *Stage-1* coarse-grained quartz. For a better evaluation of the grain size of the quartz aggregate in the map 2, the subsequent high-detailed map was considered. The grain size measured here is of 3.5 ± 2.2 μm (2.8 μm as a simple mean).

The values of grain size calculated with a root mean square are comprised in the range between 3.3 and 3.8 μm. The value of 3.3 μm has been considered to represent the mean grain size of recrystallization during the *Stage-2* deformation. The spot sizes used for the maps are compatible with calculations for this range of gran size. Anyway, the fact that all the maps shows a lot of recrystallized grains with dimensions smaller than 3.3 μm suggests that this value represent only an upper limit of the grain size. Even more the RMS is more influenced by the presence of high values, and so it depends on the accuracy of the GOS-based threshold.

3.3.4 Quadruple junctions

In both the investigated areas some quadruple junctions between quartz grains have been observed. The quartz aggregate with the highest concentration of quadruple junctions is ribbon 2 of the first map (317 recognized quadruple junction on a total of 10975 grains and

subgrains). This quartz aggregate exhibits also some alignments of grain boundaries. These features have been attributed to the contribution of grain boundary sliding to the deformation mechanisms (Tokle et al., 2019).

3.4 Discussion

3.4.1 Slip systems

The pole figures and the misorientation axis distributions for the considered quartz aggregates are not very clear, probably because the *Stage-2* CPO shows relicts orientations of the *Stage-1* mylonites. Anyway, the pole figures suggest that, differently from the *Stage-1* mylonites, the main slip system active during the deformation was not the prism <a>. This latter slip system is typically associated with high temperature or low strain rate, and thus is compatible with amphibolitic conditions of the *Stage-1*. We infer that during the *Stage-2* reactivation the main slip system was the rhomb <a>. The presence of quadruple joints and alignments of grain boundaries also suggest that reactivation occurred at a high differential stress.

3.4.2 Piezometer

For the estimate of differential stress during *Stage-2* we used the Stipp and Tullis (2003) piezometer with the EBSD-calibration proposed by Cross (2017). Since we deal with grain size far lower than 10 μm we used the "EBSD sliding resolution RMS piezometer", defined as:

$$D = 10^{4.22 \pm 0.51} * \sigma^{-1.59 \pm 0.26}$$

For the calculation we considered 3.3 ± 1.3 μm, i.e. the minimum estimated RMS grainsize. The corresponding differential stress is 205 ± 50 MPa.

4. Discussion and conclusions

4.1 Results

The aim of this work was to decipher the deformation conditions and mechanisms responsible for the development of *Stage-2* deformation structures in the metagranitoids of the Neves area by integrating field work, petrographic and microstructural analysis. The main results of the study can be summarized as follow:

- The *Stage-2* deformation structures have been recognized within 3 major *Stage-1* mylonite horizons (a few meter thick), within the dominantly undeformed metagranitoids, where they exploited the mylonitic foliation. The *Stage-2* structures include both ductile (mylonites) and brittle (pseudotachylyte) deformation structures. Pseudotachylyte were not affected by ductile shear and, therefore, postdated the mylonites.
- The shortening direction during *Stage-2* deformation has been determined to be around 354°. This value is comparable with the shortening directions during *Stage-1* (345°: Pennacchioni and Mancktelow, 2007) and during *Stage-3* (358°: Pennacchioni and Mancktelow, 2013).
- The syn-kinematic metamorphic assemblage during *Stage-2* deformation included quartz, oligoclase (Ab_{75}), biotite, epidote, and minor muscovite and K-feldspar; garnet was not stable. This assemblage is compatible with upper greenschist facies condition.
- EBSD investigation of strongly deformed and recrystallized quartz in a *Stage-2* mylonite has allowed (i) the identification of subgrain rotation as the main recrystallization mechanism, and (ii) the estimate, from the recrystallized grainsize, of a syn-kinematic differential stress of around 200 MPa (or larger). The inferred main intra-crystalline slip system active during crystal-plastic deformation of quartz was rhomb <a>.

All the above observations allow a model for *Stage-2* to be developed. As for *Stage-1* structures, localized on precursor tabular heterogeneities, strain during *Stage-2* deformation was also localized on planes of strong anisotropy ($Mylonite_{1-3}$ foliations). However, during wet, amphibolite facies conditions of *Stage-1* deformation rocks were very weak (Mancktelow and Pennacchioni, 2010) and reactivation of precursor anisotropies was possible even in cases of very low resolved shear stress. In contrast, at lower temperature during the *Stage-2* deformation stage shear localization on the precursor, highly

misoriented *Stage-1* mylonites was only possible at high stress. In contrast with *Stage-3* deformation, there is no evidence of high fluid pressures during the *Stage-2* event, and therefore yielding could not occur by development of new Andersonian fractures.

Stage-1 and *Stage-3* deformation stages have been constrained to have occurred at temperatures of 550 °C and 300 °C, respectively. A reasonable assumption for *Stage-2* deformation is a temperature of around 400 °C (upper greenschist facies) corresponding to a lithostatic pressure of around 400 MPa.

4.2 Proposed reactivation mechanism

In the shear stress-normal stress space (Fig. 26) the Mohr circle representative of *Stage-2* deformation (lithostatic pressure of 400 MPa; differential stress 200 MPa; strike-slip kinematics) is far away from both the Mohr failure envelope and the frictional sliding curve for standard static friction coefficients (ca. 0,7). This means that the rock should have been ideally stable without neither being able to fracture neither to reactivate misoriented planes of anisotropy. Even assuming a high, nearly lithostatic fluid pressure, the highly misoriented *Stage-1* foliation would be impossible to reactivate under a standard frictional coefficient unless assuming an unrealistically high tensional strength of the rock.

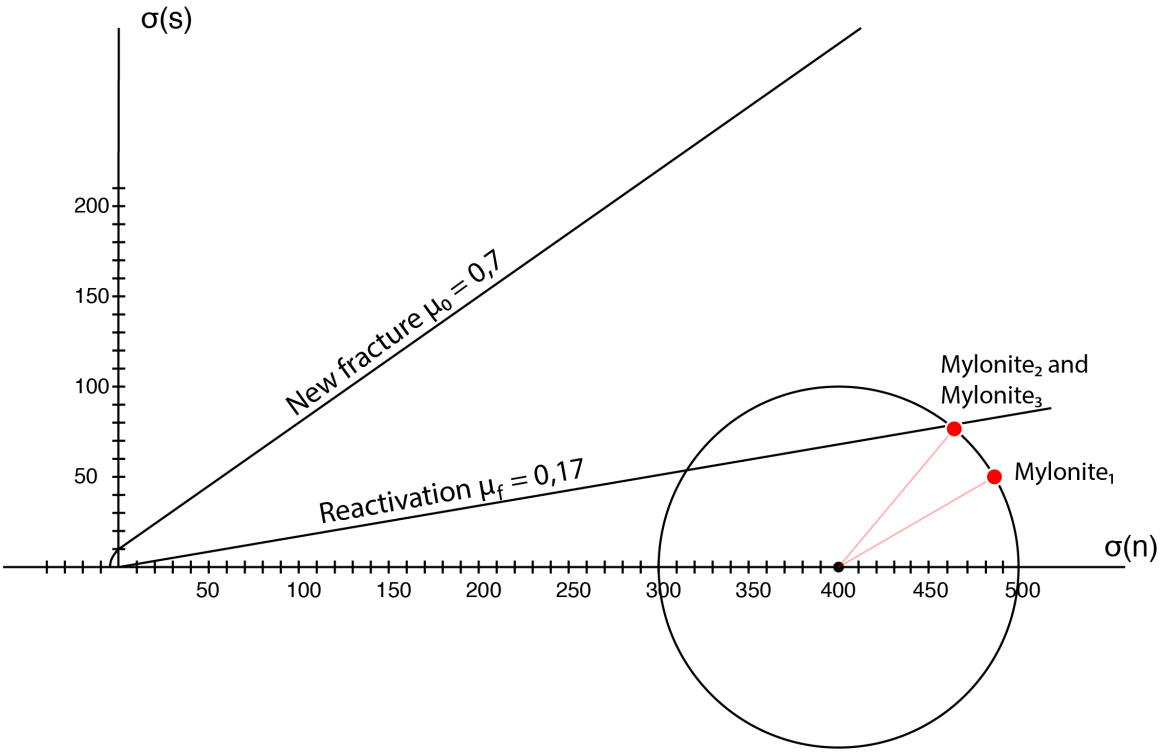

Fig. 26 Hypothetical stress conditions for the Stage-2 deformation represented in the Mohr space; the failure envelope and the reactivation envelope are reported as well as the orientations of the two main set of anisotropies

To reactivate the *Stage-1* misoriented foliation, as it is observed, the static friction coefficient must have dropped to values between 0,30 and 0,14 estimated by the slip tendency analysis. Such low values have already been observed experimentally for the reactivation of strongly foliated rocks (see *Bistacchi et al.* (2012) for a review) with at least 25-30% of phyllosilicates forming an interconnected load-supporting framework. Similar values have also been estimated for reactivation of mica-schists and phyllosilicate-rich mylonitic foliations (Massironi et al., 2011; Bistacchi et al., 2012; Bolognesi and Bistacchi, 2016, 2018; Traforti et al., 2018).

The *Stage-1* foliation of the Mylonites$_{1-3}$ is not comparable with those described in mica-schists and phyllosilicate-rich mylonitic foliations described in the above-mentioned papers. In the Neves area, in order to obtain such low frictional coefficient during *Stage-2* reactivation of *Stage-1* foliation, a progressive weakening of the rock due to mylonitic-driven rearrangement of the foliation was necessary. We infer that, during the *Stage-2* mylonitic reactivation, the ductile deformation progressively resulted in a dramatic reorganization of the fabric eventually leading to spatially continuous and interconnected weak biotite-rich layers. The final fabric reorganization leading to weakening was actually the product of mylonitization under high differential stress associated with the highly misoriented exploited anisotropy (*Stage-1* foliation).

Once the required low friction coefficients were reached over a large enough surface, the frictional slip was enabled (the Mohr reactivation envelope intersect the preexisting foliation). The initial slip produced cataclastic deformation at the slipping surface stepover that contributed to decrease the "fault" segmentation further increasing the slip area. Once the slip was sustained over a critical area a coseismic slip took place and pseudotachylytes developed. This proposed process can be seen as a self-sustained process for earthquakes nucleation in highly misoriented planes at the brittle-ductile transition.

4.3 Potential future developments

For a better understanding of the processes involved in the *Stage-2* deformation and to evaluate whether the weakening of the foliation due to rearrangement of the fabric is a reasonable hypothesis, future research should be addressed at:

- Defining more accurately the P-T condition of the *Stage-2* deformation. This will require a more detailed petrological analysis.
- Dating of the pseudotachylytes to determine the exhumation environment of *Stage-2* deformation.

- Investigating the microstructures of the composite, phyllosilicate-rich foliations providing the potential plane of weakness (low friction coefficient) allowing reactivation of highly misoriented planes.
- Investigating experimentally in triaxial apparatus the friction coefficient for reactivation of *Stage-2* mylonites.

APPENDIX

A1. Field measurements and Normalized Slip Tendency (TsN)

Mylonitic Belt	Dip	Dip direction	Trend	Plunge	TsN
1	61	187	-	-	0,14
1	65	182	-	-	0,13
1	85	181	090	16	0,19
2	82	331	057	29	0,4
2 *	77	329	061	16	0,45
2	72	332	061	18	0,47
2	79	329	053	10	0,44
2 *	79	336	-	-	-
2 *	76	347	072	11	0,36
2	69	344	-	-	-
2 *	74	334	057	24	0,44
2 *	77	340	061	16	0,38
3 *	71	328	049	22	0,5

The asterisk indicates the measurements associated with a pseudotachylyte.

In the stress inversion and TsN analysis we reject planes without a measured lineation, except for the two planes of mylonite$_1$ (to have more than one measurement for this set of planes)

A2. Quartz grains

Map	EBSD points	Total grains	Recrystallized	Relict
Map 1 - Ribbon 1	2180003	5110	4736	374
Map 1 - Ribbon 2	1097466	4593	4219	374
Map 2 - Area 1	266074	4263	2890	1373
Map 2 - Area 2	54330	260	199	61
Map 3 - detail	2923480	4669	3428	1241

(grains are reported without considering Dauphiné twinning; critical misorientation 10°)

A3. Trade Off for quartz grains populations

The trade-off curve is drawn with the number of measurements on the x-axis and the discriminating value (GOS (rad)) on the y-axis. Ideally it has an exponential shape. The knee of the curve (the furthest point from a line connecting first and last points of the curve) represent the critical threshold value to separate grains.

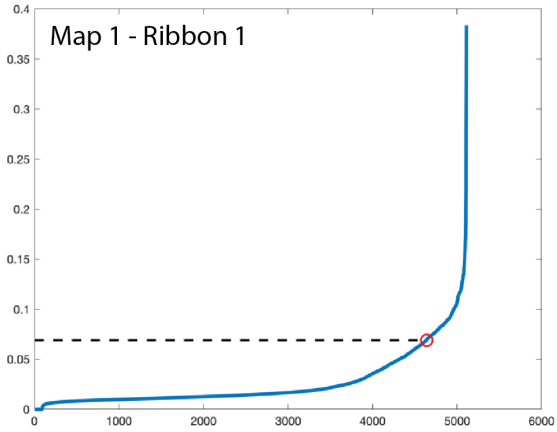

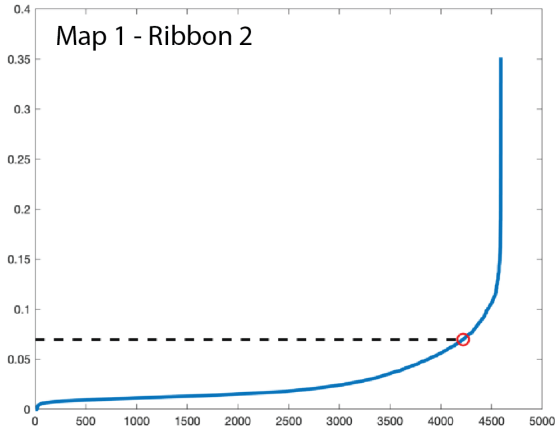

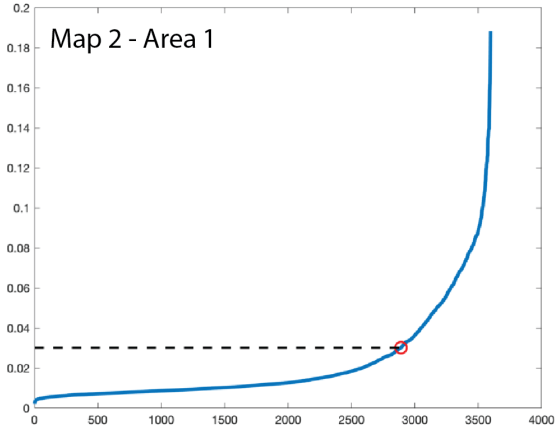

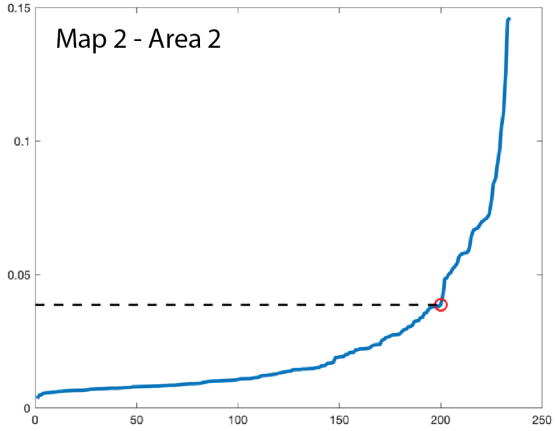

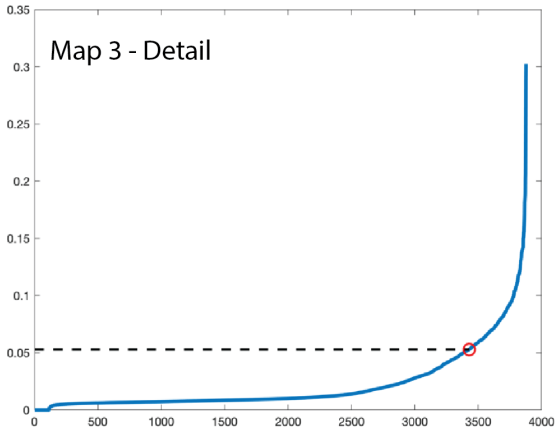

A4. Grain size distribution for the recrystallized quartz populations

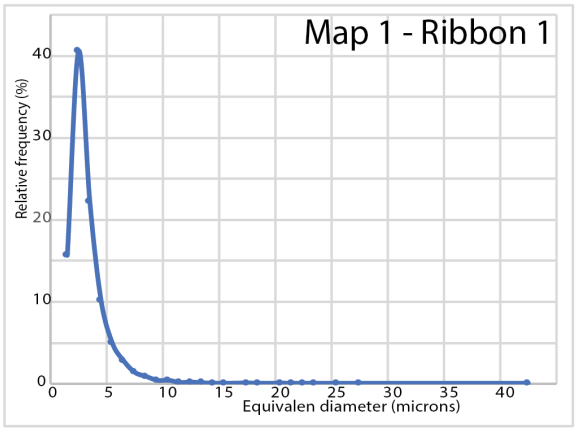

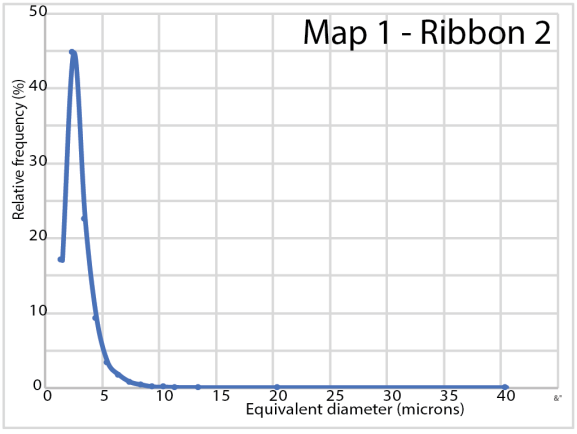

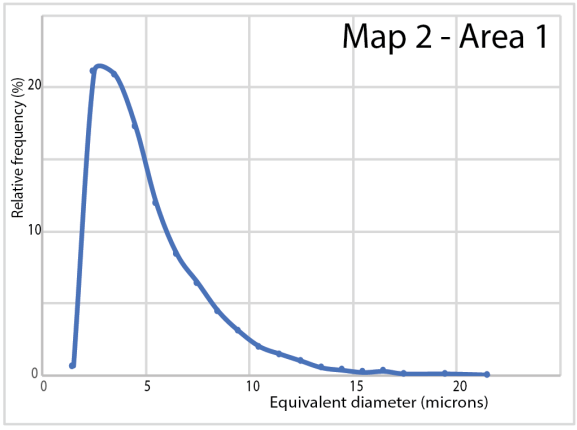

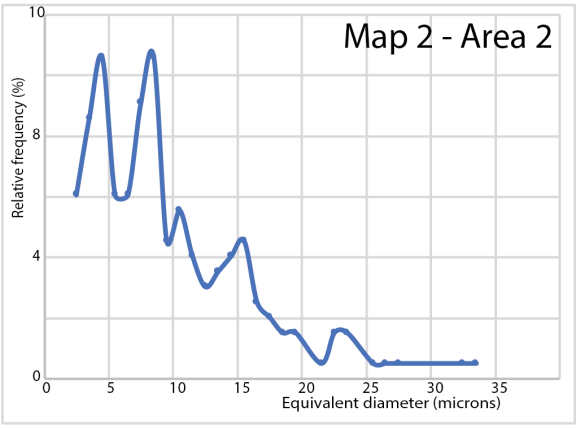

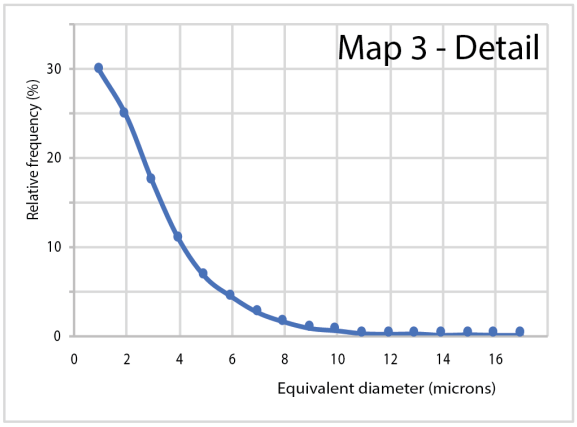

BIBLIOGRAPHY

Bachmann, F., Hielscher, R., and Schaeben, H., 2011. Grain detection from 2d and 3d EBSD data-Specification of the MTEX algorithm. Ultramicroscopy 111, 1720–1733, https://doi.org/10.1016/j.ultramic.2011.08.002

Bestmann, M., Pennacchioni, G., Nielsen, S., Göken, M., & De Wall, H., 2012. Deformation and ultrafine dynamic recrystallization of quartz in pseudotachylyte-bearing brittle faults: A matter of a few seconds. J. Struct. Geol. *38*, 21-38, https://doi.org/10.1016/j.jsg.2011.10.001

Bestmann, M., Pennacchioni, G., 2015. Ti distribution in quartz across a heterogeneous shear zone within a granodiorite: the effect of deformation mechanism and strain on Ti resetting. Lithos 227:37–56. http://dx.doi.org/10.1016/j.lithos.2015.03.009.

Bistacchi, A., Massironi, M., Menegon, L., Bolognesi, F., Donghi, V., 2012. On the nucleation of non-Andersonian faults along phyllosilicate-rich mylonite belts. Geol. Soc. Lond. Spec. Publ. 367, 185–199. https://doi.org/10.1144/SP367.13.

Bolognesi, F., Bistacchi, A., 2016. Weakness and mechanical anisotropy of phyllosilicate-rich cataclasites developed after mylonites of a low-angle normal fault (Simplon Line, Western Alps). J. Struct. Geol. 83, 1–12. http://doi.org/10.1016/j.jsg.2015.11.009.

Bolognesi, F., Bistacchi, A., 2018. A km-scale "triaxial experiment" reveals the extreme mechanical weakness and anisotropy of mica-schists (Grandes Rousses Massif, France). J. Struct. Geol. 107, 53–63. https://doi.org/10.1016/j.jsg.2017.12.001.

Cesare, B., Rubatto, D., Hermann, J., Barzi, L., 2002. Evidence for Late Carboniferous subduction-type magmatism in mafic-ultramafic cumulates of the SW Tauern window (Eastern Alps). Contributions to Mineralogy and Petrology 142, 449-464. https://doi.org/10.1007/s004100100302

Cross, A. J., Prior, D. J., Stipp, M., & Kidder, S., 2017. The recrystallized grain size piezometer for quartz: An EBSD-based calibration. Geophysical Research Letters, *44*(13), 6667-6674. https://doi.org/10.1002/2017GL073836

Delvaux, D., Sperner, B., 2003. New aspects of tectonic stress inversion with reference to the TENSOR program. Geol. Soc. Lond. Spec. Publ. *212*(1), 75-100. https://doi.org/10.1144/GSL.SP.2003.212.01.06

Delvaux, D., 2011. Win-Tensor, an interactive computer program for fracture analysis and crustal stress reconstruction. Geophysical Research Abstracts In: EGU General Assembly, Vienna, 2011, vol. 13 EGU2011-4018.

Friedrichsen, H., Morteani, G., 1979. Oxygen and hydrogen isotope studies on minerals from alpine fissures and their gneissic host rocks. Western Tauern Window (Austria). Contributions to Mineralogy and Petrology 70, 149-152. https://doi.org/10.1007/BF00374443

Hirth, G., Tullis, J., 1992. Dislocation creep regimes in quartz aggregates. J. Struct. Geol. 14, 145–159. https://doi.org/10.1016/0191-8141(92)90053-Y

Hoernes, S., Friedrichsen, H., 1974. Oxygen isotope studies on metamorphic rocks of the western Hohe Tauern area (Austria). Schweizerische Mineralogische und Petrographische Mitteilungen 54, 769-788.

Kilian, R., Heilbronner, R., 2017. Analysis of crystallographic preferred orientations of experimentally deformed Black Hills Quartzite. Solid Earth 8, 1095–1117. https://doi.org/10.5194/se- 8- 1095- 2017

Leydier, T., Goncalves, P., Lanari, P., Oliot, E., 2019. On the petrology of brittle precursors of shear zones–an expression of concomitant brittle deformation and fluid-rock interactions in the "ductile" continental crust? *Journal of Metamorphic Geology*. https://doi.org/10.1111/jmg.12504

Lisle, R. J., & Srivastava, D. C., 2004. Test of the frictional reactivation theory for faults and validity of fault-slip analysis. *Geology*, *32*(7), 569-572. https://doi.org/10.1130/G20408.1.

Magloughlin, J. F., 2005. Immiscible sulfide droplets in pseudotachylyte: Evidence for high temperature (> 1200 C) melts. Tectonophysics, *402*(1-4), 81-91. https://doi.org/10.1016/j.tecto.2004.11.011

Mainprice, D., Bachmann, F., Hielscher, R., and Schaeben, H., 2014 Descriptive tools for the analysis of texture projects with large datasets using MTEX: strength, symmetry and components. Geol. Soc. Lon. Spec. Publ., 409, 251-271 https://doi.org/10.1144/SP409.8,

Mancktelow, N.S., Pennacchioni, G., 2005. The control of precursor brittle fracture and fluid–rock interaction on the development of single and paired ductile shear zones. J. Struct. Geol. 27, 645–661. http://dx.doi.org/10.1016/j.jsg.2004.12.001.

Mancktelow, N. S., & Pennacchioni, G. (2010). Why calcite can be stronger than quartz. J. Geophys. Res. Solid Earth, *115*(B1). https://doi.org/10.1029/2009JB006526

Massironi, M., Bistacchi, A., Menegon, L., 2011. Misoriented faults in exhumed metamorphic complexes: rule or exception? Earth Planet Sci. Lett. 307, 233–239. https://doi.org/10.1016/j.epsl.2011.04.041.

Morris, A.P., Ferrill, D.A., Henderson, D.B., 1996. Slip-tendency analysis and fault reactivation. Geology 24, 275. http://dx. doi.org/10.1130/0091-7613(1996).

Papa, S., Pennacchioni, G., Angel, R. J., Faccenda, M., 2018. The fate of garnet during (deep-seated) coseismic frictional heating: The role of thermal shock. *Geology*, *46*(5), 471-474. https://doi.org/10.1130/G40077.1

Pennacchioni, G., Mancktelow, N.S., 2007. Nucleation and initial growth of a shear zone network within compositionally and structurally heterogeneous granitoids under amphibolite facies conditions. J. Struct. Geol. 29, 1757–1780. http://dx.doi.org/10. 1016/j.jsg.2007.06.002.

Pennacchioni, G., Mancktelow, N.S., 2013. Initiation and growth of strike-slip faults within intact metagranitoid (Neves area, Eastern Alps Italy). Geol. Soc. Am. Bull. 125, 1468–1483, http://dx.doi.org/10.1130/B30832.1.

Pennacchioni, G., & Mancktelow, N. S., 2018. Small-scale ductile shear zones: neither extending, nor thickening, nor narrowing. Earth-Science Reviews, *184*, 1-12. https://doi.org/10.1016/j.earscirev.2018.06.004

Prior, D. J., Mariani, E., & Wheeler, J., 2009. EBSD in the earth sciences: applications, common practice, and challenges. In *Electron backscatter diffraction in materials science* (pp. 345-360). Springer, Boston, MA. https://doi.org/10.1007/978-0-387-88136-2_26

Ranalli, G. (1995). *Rheology of the Earth*. Springer Science & Business Media.

Selverstone, J., 1985. Petrologic constraints on imbrication, metamorphism, and uplift in the SW Tauern Window, Eastern Alps. Tectonics 4, 687-704. https://doi.org/10.1029/TC004i007p00687

Selverstone, J., 1988. Evidence for east-west crustal extension in the Eastern Alps: implications for the unroofing history of the Tauern Window. Tectonics 7, 87-105. https://doi.org/10.1029/TC007i001p00087

Shigematsu, N., Prior, D. J., Wheeler, J., 2006. First combined electron backscatter diffraction and transmission electron microscopy study of grain boundary structure of deformed quartzite, J. Microsc., 224(3), 306–321, https://doi.org/10.1111/j.1365-2818.2006.01697.x

Stipp, M., Stünitz, H., Heilbronner, R., Schmid, S.M., 2002. The Eastern Tonale fault zone: A "natural laboratory" for crystal plastic deformation of quartz over a temperature range from 250 °C to 700 °C. J. Struct. Geol. 24, 1861–1884. http:// dx.doi.org/10.1016/S0191-8141(02)00035-4.

Stipp, M., Tullis, J., 2003. The recrystallized grain size piezometer for quartz. Geophys. Res. Lett. 30, 2088-2003. http://dx.doi.org/10.1029/2003GL018444.

Swanson, M. T., 1992. Fault structure, wear mechanisms and rupture processes in pseudotachylyte generation. Tectonophysics, *204*(3-4), 223-242. https://doi.org/10.1016/0040-1951(92)90309-T

Tokle, L., Hirth, G., Behr, W. M., 2019. Flow laws and fabric transitions in wet quartzite. Earth and Planetary Science Letters, *505*, 152-161. https://doi.org/10.1016/j.epsl.2018.10.017

Traforti, A., Massironi, M., Bistacchi, A., Zampieri, D., Viola, G., 2018. Slip-tendency analysis as a tool to constrain the mechanical properties of anisotropic rocks. J. Struct. Geol. 117, 136-147. https://doi.org/10.1016/j.jsg.2018.09.001

RINGRAZIAMENTI

Ringrazio innanzi tutto mamma e papà per avermi sempre supportato in questo percorso. Ringrazio il professor G. Pennacchioni per avermi dato la possibilità di portare avanti questo progetto. Ringrazio gli amici tutti, i compagni di corda e specialmente i coinquilini per i cinque (o sei) anni passati sotto lo stesso tetto. Un ringraziamento speciale va a Tommaso, che a forza di sentirmi parlare della tesi ormai probabilmente ne capisce più di me. E infine, ma certo non meno importante, ringrazio Elena per esserci sempre.